Christoph Stolz, BSc.

Estimation of second-degree spherical harmonics with modified Euler-Liouville equation

Master's Thesis

to achieve the university degree of

Diplom-Ingenieur

Master's degree programme: Geomatics Science

submitted to

Graz University of Technology

Supervisor

Univ.-Prof. Dr.Ing. Torsten Mayer-Gürr

Institute of Geodesy

Graz, May 2019

Affidavit

I declare that I have authored this thesis independently, that I have not used other than the declared sources/resources, and that I have explicitly indicated all material which has been quoted either literally or by content from the sources used. The text document uploaded to TUGRAZonline is identical to the present master‘s thesis.

Date	Signature

Abstract

Spherical harmonics and their correlating coefficients, which are measured by numerous methods, define the Earth's gravity field in the context of scientific consideration.
The Euler-Liouville differential equation represents the equation of motion for the rotation of a dynamic Earth and describes the mutual influences between the gravity field and rotation vector due to the time-varying inertia tensor, which is defined by second-degree coefficients. The formula calculated the angular velocity and was applied to simulate an Earth's rotation vector by numerical integration as an initial value problem. The integrated vector was the foundation of this thesis.
Furthermore, the integration progress was modified to determine the impact of temporal variations of each parameter, which was implemented as numerical derivation. The parameters of the spherical harmonic coefficients were estimated per month, in contrary to initial values of the rotation vector and Love number regarding an anelastic Earth. Various parameter combinations were considered at the linearised adjustment and validated concerning a solution of Satellite Laser Ranging (SLR) observations.

In conclusion, the estimated zeroth order cosine coefficients (c_{20}), as well as second-order cosine and sine coefficients (c_{22}, s_{22}), contained a constant offset. Furthermore, the determined variances were in disagreement in comparison to those of the reference solution. The most suitable results were obtained by the tesseral coefficients (c_{21}, s_{21}), due to a viable coherence to the rotation vector. Thereby solutions with the further determination of the Love number were the most fitting in terms of their approach towards their reference coefficients, although differences of coefficient s_{21} were less significant than those of coefficient c_{21}.

Zusammenfassung

Im Kontext wissenschaftlicher Betrachtungen wird das Gravitationsfeld der Erde mithilfe von Koeffizienten, in Abhängigkeit zu Kugelflächenfunktionen, ermittelt. Diese wiederum können durch eine Vielzahl von unterschiedlichsten Methoden bestimmt werden.
Die wechselseitige Beeinflussung von Gravitationsfeld und Erdrotationsachse wird anhand der Euler-Liouville Differentialgleichung beschrieben, welche die Bewegungsgleichung für die Rotation der dynamischen Erde darstellt. Als Ausgangspunkt der vorliegenden Arbeit wurde diese zur Simulation eines Erdrotationsvektors anhand numerischer Integration mit Startwertproblem verwendet.
Um die Auswirkungen zeitlicher Differenzen zu bestimmen, wurden hierfür die numerische Ableitung der jeweiligen Einflussgrößen der Simulation entsprechend modifiziert und der Kugelflächenfunktionskoeffizient – anders als der reale und imaginäre Teil der Love'schen Zahl oder der Initial-Vektor der Erdrotation – monatlich bestimmt. Die so ermittelten Zuschläge des linearisierten Ausgleiches wurden daraufhin abermals mithilfe einer Lösung der SLR-Beobachtungen wissenschaftlich hinterfragt und diverse Ergebnisse möglicher Parameterkombinationen innerhalb der Schätzung einbezogen.

Als Fazit wird festgehalten, dass aufgrund der konstanten Abweichungen zur Nullstelle von einer Bestimmung der monatlichen Zuschläge des jeweiligen Kosinus Koeffizienten nullter Ordnung (c_{20}) wie auch der Kosinus und Sinus Koeffizient zweiter Ordnung (c_{22}, s_{22}) abzusehen ist. Ferner sind die dabei bestimmten Varianzen im Vergleich zur Referenz zu unspezifisch. Von den mithilfe des Erdrotationsvektors untersuchten Koeffizienten zeigen sich bei den tesseralen Koeffizienten (c_{21}, s_{21}) die besten Eigenschaften. Die in Kombination mit der Love'schen Zahl ermittelten Lösungen passen sich in Hinblick auf ihre Referenzkoeffizienten am besten an, gleichwohl die berechneten Differenzen des Koeffizienten s_{21} weniger prägnant ausfallen als jene von c_{21}.

Contents

1 Introduction

The Earth is a dynamic system, distinguished into three fields: the Earth's geometry, orientation and gravity field. The cause of variations in these areas has multiple sources, such as the gravitational forces of bodies within the solar system. Additionally, the variations have mutual influences on each other. Monitoring and understanding alterations are the foundation to provide an exact reference frame, which serves as a base for scientific and societal applications. The changes are monitored by the Global Geodetic Observing System (GGOS), GGOS (2016).

This thesis focuses on the Earth's rotation, a fundamental part for the definition of the reference system's origin. Therefore, the behaviour has to be observed continuously with use of different techniques including Very Long Baseline Interferometry (VLBI), Satellite/Lunar Laser Ranging (SLR/LLR) and Global Navigation Satellite Systems (GNSS) (Moritz et al., 1987, p. 323ff.). The second aspect of this paper relates to the spherical harmonic coefficients, which define a gravity field model.
The state of the art approach towards determining gravity field models is an integration of multiple techniques. The practised methods provide different levels of accuracies for individual coefficients, which further depend on their resolution – represented by degree and order of the spherical harmonics.
The relation of the rotation vector to the mass distribution can be stated by a modified Euler-Liouville equation. The objective of this thesis was to investigate a possible additional method to determine coefficients of second-degree spherical harmonics. Gaining another source to resolve spherical harmonic coefficients and adding further observations to the determination of a gravity field model would improve these results as long as the certainties are adequate to other methods. Measurements of SLR observations provide the highest accuracies regarding second-degree spherical harmonics and act as a quantification reference.

2 Theory of the Earth's rotation

2.1 Reference frames

The variations of the rotation vector are divided into two areas: the study respecting an Earth-fixed reference frame and the study respecting a Space-fixed reference frame (Dehant and Mathews, 2015). This thesis focuses on the former, which is described by two parameters:

- polar motion is defining the orientational changes of the rotation vector in relation to the polar axis of the frame
- Length of Day (LOD) is representing the absolute value of the rotation vector, thus the angular velocity

The rotation vector changes its orientation in addition to the mentioned polar motion that is observed in an Earth-fixed frame as well as in a Space-fixed frame. These variations are known as precession and nutation (Dehant and Mathews, 2015, p. 2f.). Though this thesis discusses the variation in an Earth-fixed system, it is still of significance to acknowledge the Space-fixed system motion parameters and even more so the transformation of one system into the other. Due to the gravitational forces of the Moon and Sun, referred to as lunisolar in combination, which is influencing the parameters in either system. Therefore it is necessary to transform the lunisolar Space-fixed coordinates for an Earth-fixed frame.

Transforming from a Celestial Reference System (CRS) to a Terrestrial Reference System (TRS) can be enunciated by a series of multiplications of elementary rotation matrices (Dehant and Mathews, 2015, p. 88ff.). Since orientational alteration in the systems changes relative to one another. The motion parameters are expressed by individual matrices that are rotational sets of different axes

$$\boldsymbol{x}_{CRS} = \boldsymbol{R}_{TRS}^{CRS}(t) \cdot \boldsymbol{x}_{TRS}, \tag{2.1}$$

$$\boldsymbol{R}_{TRS}^{CRS}(t) = \boldsymbol{Q}(t) \cdot \boldsymbol{R}(t) \cdot \boldsymbol{W}(t). \tag{2.2}$$

The polar motion is covered with the matrix $\boldsymbol{W}(t)$, which is the rotation from a terrestrial system of a specific epoch into a true terrestrial reference system:

$$\boldsymbol{W}(t) = \boldsymbol{R}_y(x_p)\boldsymbol{R}_x(y_p). \tag{2.3}$$

The next rotation $\boldsymbol{R}(t)$ describes the transformation of a true celestial equatorial to a true terrestrial system, each at a specific time. Therefore the true angle between the true vernal equinox and the Greenwich meridian is required, also known as the Greenwich Apparent Sidereal Time (GST). This hour angle also contains Earth variations as well as the motion of the vernal equinox,

$$\boldsymbol{R}(t) = \boldsymbol{R}_z(-GST). \tag{2.4}$$

The last rotation $\boldsymbol{Q}(t)$ manages the precession and nutation. Splitting up into the precession $\boldsymbol{P}(t)$ and nutation $\boldsymbol{N}(t)$ matrices gives:

$$\begin{aligned} \boldsymbol{Q}(t) &= \boldsymbol{N}(t)\boldsymbol{P}(t), \\ \boldsymbol{P}(t) &= \boldsymbol{R}_z(\zeta_a)\boldsymbol{R}_y(-\theta_a)\boldsymbol{R}_z(z_a), \\ \boldsymbol{N}(t) &= \boldsymbol{R}_x(-\epsilon_s)\boldsymbol{R}_z(\Delta\psi)\boldsymbol{R}_x(\epsilon_s + \Delta\epsilon). \end{aligned} \tag{2.5}$$

These matrices contain the equatorial precession parameters (ζ_a, θ_a, z_a) (Lieske et al., 1977) and celestial pole offsets $(\Delta\psi, \Delta\epsilon)$. Former ones are published by the International Astronomical Union (IAU). The celestial pole offset parameters are two of five Earth Orientation Parameters (EOP). The other ones are the polar motion (x_p, y_p) used in Eq. (2.3) and the Universal Time offset $(\Delta UT1)$. The latter one is needed to calculate the GST of Eq. (2.4). The International Earth Rotation and Reference System Service (IERS) monitors and publishes these on daily and they are used for rotational transformation considering all irregularities between the terrestrial and the celestial system.

The coordinates determining the position of Sun and Moon are DE421 ephemeris published by the Jet Propulsion Laboratory (JPL) (JPL, 2014a) for the terrestrial reference frame. Therefore there was no demand for any transformation as a part of the thesis. Summarising the major features provides valuable insight for understanding the complex motions of the Earth's rotation. Further references regarding the topic of precession and nutation are Dehant and Mathews (2015) and IERS (2013).

2.2 Polar motion

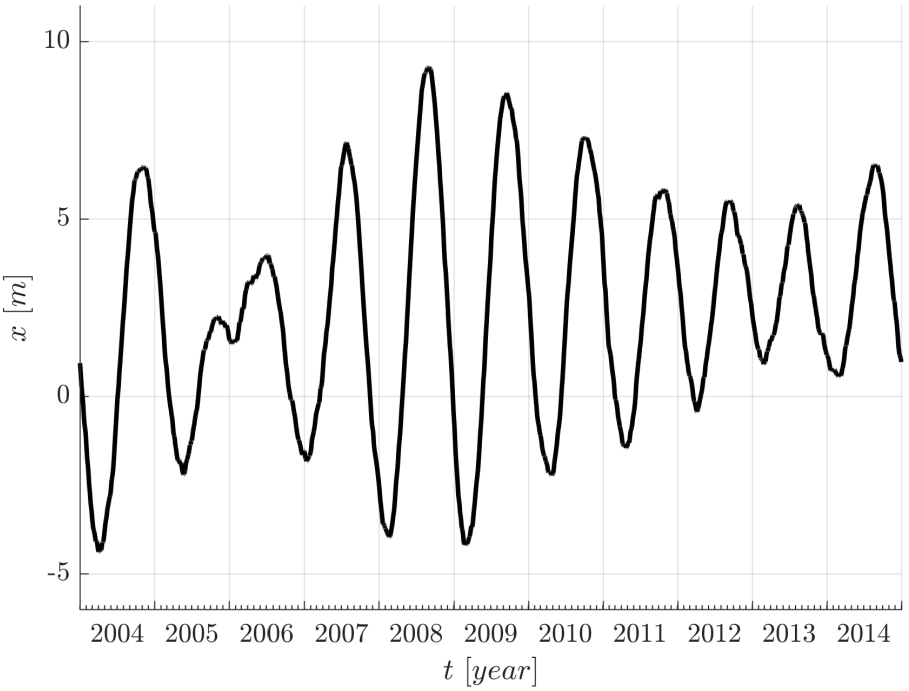

Figure 2.1: Daily polar motion along the x-axis computed by the observed rotation vector between the years 2004 and 2014.

Figures 2.1 and 2.2 shows the determined polar motion and its period of approximately 435 days. Named after its discoverer, Seth Carlo Chandler, the Chandler period (Moritz et al., 1987, p. 48) is a damped oscillation. The Earth is in constant motion due to the effects of internal and external forces (Moritz et al., 1987, p. 280ff.) – the dynamic system Earth. Variances of the geometry or gravity field of the Earth, caused by atmospheric mass shift, tides, and earthquakes amongst others, have an impact on the rotation vector due to changes of torque or inertia vector and vice versa.
Additionally, the rotation axis of the Earth is not coincidental with the body axis, which leads to a wobbling motion of the rotation axis. The oscillation period of a comparable rigid body in size of the Earth would last 305 days and is known as the Euler period (Moritz et al., 1987, p. 48). The polar motion is

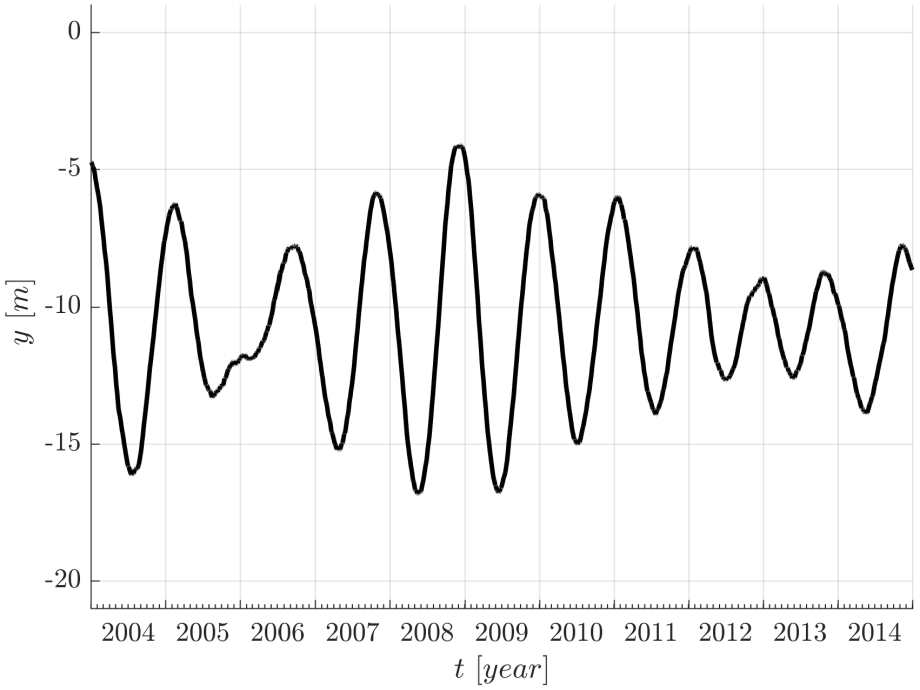

Figure 2.2: Daily polar motion along the y-axis computed by the observed rotation vector between the years 2004 and 2014.

calculated by using the following equations in relation to the components of Earth rotation vector ω_x and ω_y in rad/s

$$\begin{aligned} x_p(t) &= \frac{R}{\Omega_N}\omega_x(t), \\ y_p(t) &= \frac{R}{\Omega_N}\omega_y(t). \end{aligned} \tag{2.6}$$

The radius of the Earth R and nominal Earth rotation Ω_N is defined by

$$\begin{aligned} R &= 6378136.6m, \\ \Omega_N &= 7.2921151467064 \cdot 10^{-5 rad/s}. \end{aligned} \tag{2.7}$$

Figures 2.1 and 2.2 displays the average polar motion of each day, derived from the rotation vector. The relative motions in respect to the Earth-fixed

reference frame vary between $-4\,\mathrm{m}$ and $+9\,\mathrm{m}$ at the x-axis. At the orthogonal y-axis the variations are between $-17\,\mathrm{m}$ and $-4\,\mathrm{m}$. Both indicate the offset of the rotation axis to the Earth's body axis at the relating time frame between January 1$^{\mathrm{st}}$ 2004 and December 31$^{\mathrm{th}}$ 2014. The most obvious oscillation shows the Chandler period. The amplitude of the period is inconsistent, and the signal is further affected by a beat, as seen at the turn between the years 2005 and 2006. This shift leads to the extinction of the upcoming ascending peak followed by another ascending one. The time series's analytical trends are hardly noticeable ($10^{-5}\,\mathrm{m}$) - the migration movement of the rotation axis (IERS, 2013) is not detectable – due to the shortness of time. Figure 2.3 illustrates the polar motion of both axes including the oscillation of the Chandler period as well as the beat of approximate 6.4 years, which is a result of an annual period overlaying with the Chandler signal (Seitz, 2004, p. 12f.).

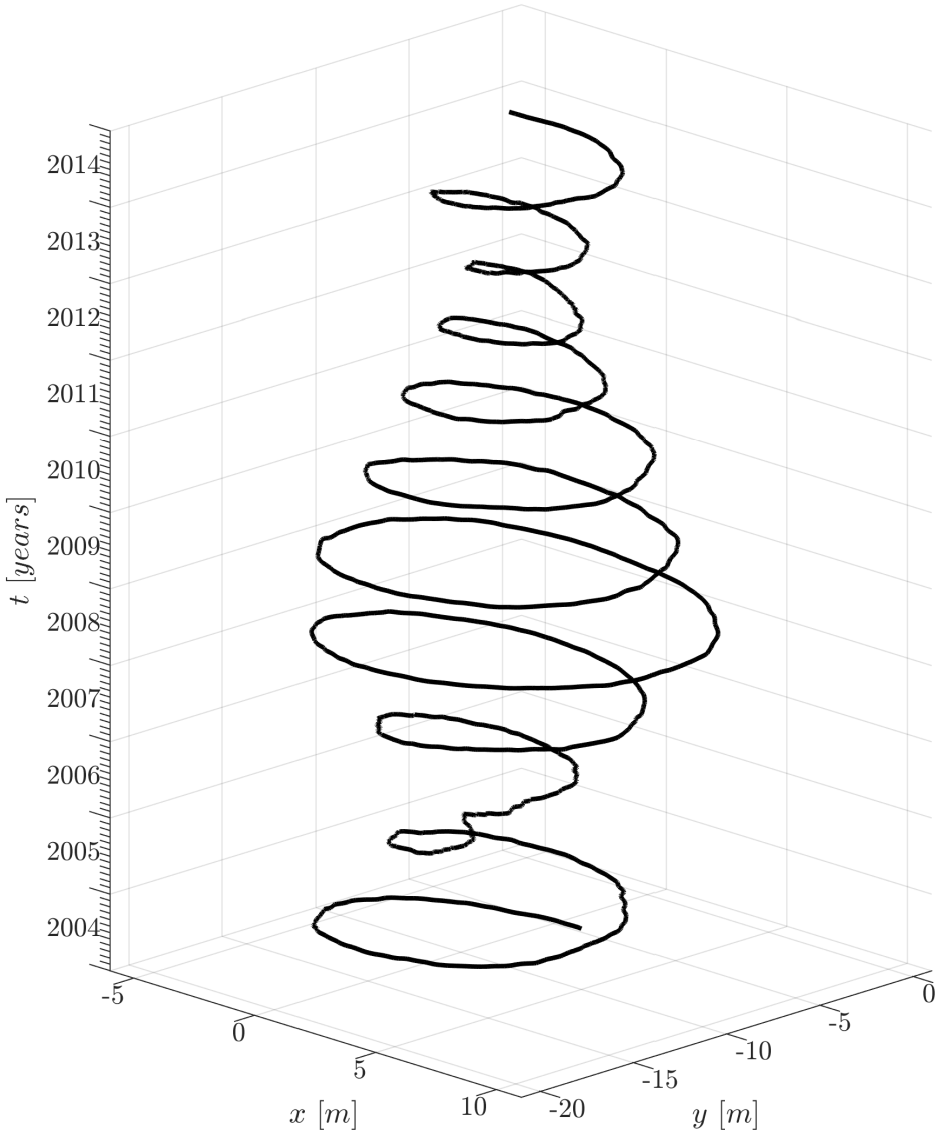

Figure 2.3: Daily polar motion along x- and y-axis computed by the observed rotation vector between the years 2004 and 2014.

2.3 Length of day

The time needed for one full Earth rotation varies at a daily base, stated by the length of day variations (ΔLOD) in the range of milliseconds, characterised in Fig. 2.4. The differences are defined using the constants of Eq. (2.7):

$$\Delta LOD = 86.400s \frac{\Omega_N - \omega_z}{\Omega_N}. \tag{2.8}$$

ΔLOD is dominated by an annual signal in addition to high-frequent variations. Traceable influences on the length of day variations are assumably caused by the Earth's core, mantle and its generated magnetic field (Seitz and Schuh, 2010, p. 196f.).

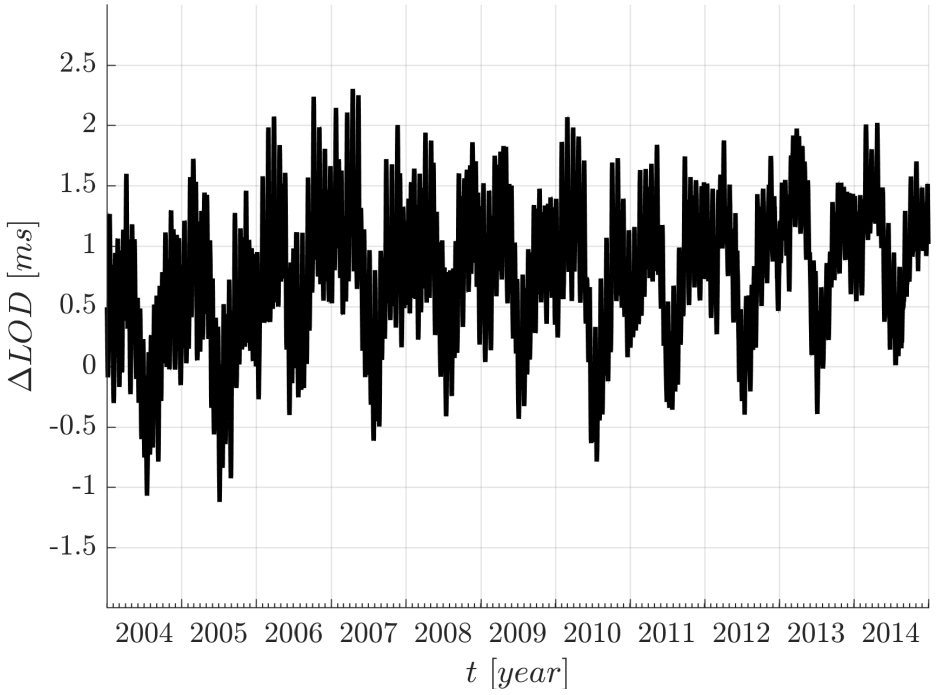

Figure 2.4: Daily ΔLOD computed by the observed rotation vector between the years 2004 and 2014.

2.4 Euler-Liouville equation

How a rigid body reacts to external torques within a rotating reference system is mathematically defined by the Euler's rotation equation (Moritz et al., 1987, p. 46ff.):

$$\boldsymbol{T}\dot{\boldsymbol{\omega}} + \boldsymbol{\omega} \times \boldsymbol{T}\boldsymbol{\omega} = \boldsymbol{M}. \tag{2.9}$$

The sum of external torques of Sun and Moon is represented as $\boldsymbol{M}$, known as lunisolar torques. Variable $\boldsymbol{T}$ stands for the inertia tensor of Earth as $\boldsymbol{\omega}$ stands for its rotation vector of the rotating system. The inertia tensor is understood as the Earth's mass distribution along the system's axis, therefore is $\boldsymbol{T}$ is a 3×3 matrix. Choosing a principal coordinate system (Dehant and Mathews, 2015, p. 18) leads to a diagonal matrix:

$$\boldsymbol{T}_{PCS} = \begin{pmatrix} A & 0 & 0 \\ 0 & B & 0 \\ 0 & 0 & C \end{pmatrix}. \tag{2.10}$$

As a simplification, the tensor of the Earth can be assumed to be equal to the tensor of an ellipsoid of rotation. The diagonal elements A and B are therefore identical, and all elements are constant for a rigid body.
The inertia tensor $\boldsymbol{T}$ multiplied by the rotation vector $\boldsymbol{\omega}$ equals the angular momentum $\boldsymbol{L}$. The change of the angular momentum over time (first derivation) is the physical quantity of the torque $\boldsymbol{M}$

$$\dot{\boldsymbol{L}} = \boldsymbol{M}. \tag{2.11}$$

Replacing the inertia tensor in the Euler's rotation equation with the angular momentum in a body tied system results in:

$$\frac{d\boldsymbol{L}}{dt} + \boldsymbol{\omega} \times \boldsymbol{L} = \boldsymbol{M}. \tag{2.12}$$

The angular momentum of a rotating non-rigid body is the sum of the time variant inertia tensor multiplied by rotation vector and a motion term $\boldsymbol{h}$,

$$\boldsymbol{L} = \boldsymbol{T} \cdot \boldsymbol{\omega} + \boldsymbol{h}. \tag{2.13}$$

The latter results from the mass distribution in relation to the rotating system, known as a relative angular momentum. The Euler-Liouville equation (Moritz et al., 1987, p. 122ff.) indicates time variant changes of the rotation vector of a deformable body within a rotating system:

$$\boldsymbol{T}\dot{\boldsymbol{\omega}} + \boldsymbol{\omega} \times (\boldsymbol{T}\boldsymbol{\omega}) + \frac{D\boldsymbol{T}}{Dt}\boldsymbol{\omega} + \boldsymbol{\omega} \times \boldsymbol{h} + \frac{D\boldsymbol{h}}{Dt} = \boldsymbol{M}. \tag{2.14}$$

Restructured in order to calculate the angular velocity of the Earth leads to the ordinary differential equation:

$$\dot{\boldsymbol{\omega}} = \boldsymbol{T}^{-1}\left[\boldsymbol{M} - \frac{D\boldsymbol{T}}{Dt}\boldsymbol{\omega} - \boldsymbol{\omega} \times (\boldsymbol{T}\boldsymbol{\omega}) - \boldsymbol{\omega} \times \boldsymbol{h} - \frac{D\boldsymbol{h}}{Dt}\right]. \tag{2.15}$$

Initially used to simulate the Earth's rotation vector by numerical integration as an initial value problem. Every variable in the Euler-Liouville equation is time-related:

$$\dot{\boldsymbol{\omega}} = \dot{\boldsymbol{\omega}}(t), \boldsymbol{\omega} = \boldsymbol{\omega}(t), \boldsymbol{T} = \boldsymbol{T}(t), \boldsymbol{M} = \boldsymbol{M}(t), \boldsymbol{h} = \boldsymbol{h}(t). \tag{2.16}$$

2.5 Spherical harmonics

The gravitational forces of Earth, Sun, Moon and the centrifugal force of Earth's rotation lead to the gravity field. Due to the improvement of space techniques and unique satellite missions increased accuracies and a higher resolution of modelled gravity fields are achieved. These gravity models are defined by spherical harmonics and related coefficients, which are calculated and published by institutes and teams around the globe. The second-degree coefficients of a spherical harmonic expansion are directly related to the inertia tensor

$$\boldsymbol{T} = \begin{pmatrix} A & D & E \\ D & B & F \\ E & F & C \end{pmatrix}. \tag{2.17}$$

The inertia tensor $\boldsymbol{T}$ is altered in terms of second-degree spherical harmonic coefficients. The trace cannot be determined by the gravitational potential and

is further stated by tr. Adjusting the inertia tensor by using normalised basis functions as well as the gravitational potential and integrating along the related axis of the inertia product results in:

$$\boldsymbol{T} = \sqrt{\frac{5}{3}} MR^2 \begin{pmatrix} \frac{1}{\sqrt{3}}c_{20} - c_{22} & -s_{22} & c_{21} \\ -s_{22} & \frac{1}{\sqrt{3}}c_{20} + c_{22} & s_{21} \\ -c_{21} & -s_{21} & \frac{2}{\sqrt{3}}c_{20} \end{pmatrix} + \frac{1}{3} \begin{pmatrix} tr & 0 & 0 \\ 0 & tr & 0 \\ 0 & 0 & tr \end{pmatrix}. \quad (2.18)$$

The explicit derivation of six elements of the inertia tensor are given by Seitz (2004, p. 25f.).

2.6 Rotation deformation

The varying rotation vector has a significant impact on the centrifugal potential of the Earth and further to its deformation. This rotational deformity is defined by changes in the inertia tensor and coefficients of spherical harmonics of to the gravitational potential. The previous tensor of the Liouville equation is split up regarding the effects of pole tides $\boldsymbol{T}_R$ and gravitational potential $\boldsymbol{T}_G$:

$$\boldsymbol{T}(t) = \boldsymbol{T}_G(t) + \boldsymbol{T}_R(t). \quad (2.19)$$

Analog to Eq. (2.18) is the rotation deformation's tensor:

$$\boldsymbol{T}_R = \sqrt{\frac{5}{3}} MR^2 \begin{pmatrix} 0 & 0 & -\Delta c_{21} \\ 0 & 0 & -\Delta s_{21} \\ -\Delta c_{21} & -\Delta s_{21} & 0 \end{pmatrix}. \quad (2.20)$$

The coefficient differences of the spherical harmonics are:

$$\begin{aligned} \Delta c_{s21}(t) &= -\sqrt{\frac{3}{5}} \frac{\Omega_N R^3}{3GM} \left(k^{Re}\omega_x + k^{Im}\omega_y \right), \\ \Delta s_{s21}(t) &= -\sqrt{\frac{3}{5}} \frac{\Omega_N R^3}{3GM} \left(k^{Re}\omega_y + k^{Im}\omega_x \right). \end{aligned} \quad (2.21)$$

The variables of k are referring to the Love number, a dimensionless parameter that characterises the deformability of the Earth. Three different Love numbers are defined to measure a planetary body behaviour in response to potential changes (Dehant, Defraigne, et al., 1999). The real k^{Re} and imaginary k^{Im} are parts of the complex Love number relating to the properties of an anelastic earth. The spherical harmonic coefficient differentials from Eq. (2.21) are substituted in (2.20) and lead to the matrix:

$$\boldsymbol{T}_R(t) = \frac{\Omega_N R^5}{3G} \begin{pmatrix} 0 & 0 & k^{Re}\omega_x + k^{Im}\omega_y \\ 0 & 0 & k^{Re}\omega_y - k^{Im}\omega_x \\ k^{Re}\omega_x + k^{Im}\omega_y & k^{Re}\omega_y - k^{Im}\omega_x & 0 \end{pmatrix}. \quad (2.22)$$

The derivative parts of the inertia tensor (Eq. (2.15)) are further distinguished and rearranged by putting the tensor in relation to the rotation deformation $\boldsymbol{T}_R$ on the left side next to the total inertia tensor $\boldsymbol{T}$:

$$\boldsymbol{T}\dot{\boldsymbol{\omega}} + \frac{D\boldsymbol{T}_R}{Dt}\boldsymbol{\omega} = \boldsymbol{M} - \frac{D\boldsymbol{T}_G}{Dt}\boldsymbol{\omega} - \boldsymbol{\omega} \times (\boldsymbol{T}\boldsymbol{\omega}) - \boldsymbol{\omega} \times \boldsymbol{h} - \frac{D\boldsymbol{h}}{Dt}. \quad (2.23)$$

Assuming the Earth's rotation vector by $\omega_x = \omega_y = 0$ and $\omega_z = \Omega_N$ (in a first order approxmiation) leads to following simplification:

$$\frac{D\boldsymbol{T}_R}{Dt}\boldsymbol{\omega} = \frac{\Omega_N^2 R^5}{3G} \begin{pmatrix} k^{Re} & k^{Im} & 0 \\ -k^{Im} & k^{Re} & 0 \\ 0 & 0 & 0 \end{pmatrix} \begin{pmatrix} \dot{\omega_x} \\ \dot{\omega_y} \\ \dot{\omega_z} \end{pmatrix}. \quad (2.24)$$

Combining with the total inertia tensor produces matrix:

$$\boldsymbol{F} = \boldsymbol{T} + \frac{\Omega_N^2 R^5}{3G} \begin{pmatrix} k^{Re} & k^{Im} & 0 \\ -k^{Im} & k^{Re} & 0 \\ 0 & 0 & 0 \end{pmatrix}. \quad (2.25)$$

The substitution of $\boldsymbol{F}$ and the rearrangement of the Euler-Liouville equation in regards to the differential rotation vector element gives its implemented form:

$$\dot{\boldsymbol{\omega}} = \boldsymbol{F}^{-1} \left[\boldsymbol{M} - \frac{D\boldsymbol{T}_G}{Dt}\boldsymbol{\omega} - \boldsymbol{\omega} \times (\boldsymbol{T}\boldsymbol{\omega}) - \boldsymbol{\omega} \times \boldsymbol{h} - \frac{D\boldsymbol{h}}{Dt} \right]. \quad (2.26)$$

3 Simulation

3.1 Introduction

This chapter is about the calculation of a simulated Earth rotation vector that builds the foundation of the developed algorithm. The result of the Euler-Liouville equation is used in a numeric integration in order to model the Earth's rotation for the time frame of the observed rotation vector, lunisolar positions and spherical harmonic coefficients. The following data was processed:

- position of Sun and Moon relatively to the Earth-fixed reference frame from DE421 ephemeris (JPL, 2014a)
- second-degree spherical harmonic coefficients of a time variable gravity field
  - daily filtered Gravity Recovery and Climate Experiment (GRACE) data from ITSG-Grace 2016 solutions (Mayer-Gürr et al., 2016) with high frequency variations of the AOD1B RL05 model (Flechtner et al., 2014)
  - potential variations by Earth tides according to the IERS2010 conventions (Petit et al., 2010) and ocean tides from the EOT11a model (Savcenko et al., 2012)
- observed Earth rotation vector from the IERS EOP 08 C04 series (Bizouard et al., 2019)

The period under review was from 01-01-2004 to 01-01-2015 with a sampling rate of one hour and provided constants of the algorithm as listed in Tab. 3.1.

Table 3.1: Processed constants in the algorithm.

Parameter		Value
k^{Re}	real part of Love number	0.3077
k^{Im}	imaginary part of Love number	0.0036
G	gravitational constant	$6.674 \times 10^{-11}\,\mathrm{m}^3/\mathrm{kg}/\mathrm{s}^2$
GM_{sun}	gravitational parameter Sun	$1.327\,124\,420\,76 \times 10^{20}\,\mathrm{m}^3/\mathrm{s}^2$
GM_{moon}	gravitational parameter Moon	$4.902\,777\,9 \times 10^{12}\,\mathrm{m}^3/\mathrm{s}^2$
M	mass of the Earth	$5.9737 \times 10^{24}\,\mathrm{kg}$
R	radius of the Earth	$6.378\,136\,6 \times 10^{6}\,\mathrm{m}$
$\bar{A} = \bar{B}$	moments of inertia	$0.3296108 \cdot MR^2$
$\bar{C}$	moment of inertia	$0.3307007 \cdot MR^2$

3.2 Earth's rotation model

In order to solve the modified Euler-Liouville equation numerically the initial value $\boldsymbol{\omega}(t = 1)$ was set as observations of the first epoch ($t = 1$) of the provided Earth rotation vector $\boldsymbol{\omega_0}$:

$$\boldsymbol{\omega}(t = 1) = \boldsymbol{\omega_0} = \begin{pmatrix} \omega_0^x \\ \omega_0^y \\ \omega_0^z \end{pmatrix}. \tag{3.1}$$

The torque $\boldsymbol{M}$ represents the total torques of third bodies ($\boldsymbol{M}_{sun} + \boldsymbol{M}_{moon}$). These are independent of the Earth rotation itself and were calculated in advance for every epoch by using element-wise vector operations:

$$\boldsymbol{M}_j = \frac{3GM_j}{r_j^5} \begin{pmatrix} y_j z_j(\bar{C} - \bar{B}) \\ x_j z_j(\bar{A} - \bar{C}) \\ x_j y_j(\bar{B} - \bar{A}) \end{pmatrix}. \tag{3.2}$$

Sun and Moon were implemented in the form of j, according to gravitational parameter GM, the position coordinates x_j, y_j, z, and the distance

$$r_j = \sqrt{x_j^2 + y_j^2 + z_j^2}. \tag{3.3}$$

The motion term $\boldsymbol{h}$ is modelled by the relative angular momentum, and the data is published by the German Centre of Geoscience (GFZ), Dobslaw et al. (2018).

The effective angular momentum (EAM) is defined by using the required motion term and describes the mass distribution above the Earth's surface. The data is available for atmosphere, dynamic ocean and continental hydrosphere in a sampling rate of three hours. Therefore the data between 2004 and 2015 was interpolated to match the temporal resolution of one hour. The motion term was computed by the total of the three EAMs, represented by vector $\boldsymbol{\chi}$ with the relation to the motion term

$$\begin{pmatrix} h_x \\ h_y \\ h_z \end{pmatrix} = \begin{pmatrix} \frac{\Omega_N(\bar{C}-\bar{A})}{1.610}\chi_1 \\ \frac{\Omega_N(\bar{C}-\bar{A})}{1.610}\chi_2 \\ \frac{\Omega_N \bar{C}}{1.125}\chi_3 \end{pmatrix}. \tag{3.4}$$

The calculation of the time series of motion terms as well as the inertia tensor of gravitational effects $\boldsymbol{T}_G$ was optimised with the use of element-wise vector operations, analogue to $\boldsymbol{M}$. The derivation parts of $\boldsymbol{h}$ and $\boldsymbol{T}_G$ were numerically generated by the mean differences of two adjacent epochs to t

$$\begin{aligned} \frac{D\boldsymbol{T}_G}{Dt}(t) &= \frac{\boldsymbol{T}_G(t+1) - \boldsymbol{T}_G(t-1)}{2 \cdot 3600}, \\ \frac{D\boldsymbol{h}}{Dt}(t) &= \frac{\boldsymbol{h}(t+1) - \boldsymbol{h}(t-1)}{2 \cdot 3600}. \end{aligned} \tag{3.5}$$

Start and end values were computed using only one adjacent epoch for the numerical derivation, due to the missing values. The denominator of the fractions considered the transformation from one hour to seconds since the angular velocity is defined in radian per seconds.

3.3 Numeric integration

For integrating the rotation vector a Euler-Integration (Griffiths et al., 2010, p. 19ff.), with a step size of one hour, was used:

$$\boldsymbol{\omega}(t+1) = \boldsymbol{\omega}(t) + \dot{\boldsymbol{\omega}}(t)\Delta t. \tag{3.6}$$

The following terms depended on the modelled Earth rotation vector and were determined within the numerical integration loop:

$$\boldsymbol{F} = \boldsymbol{F}(\boldsymbol{T}), \boldsymbol{T} = \boldsymbol{T}(\boldsymbol{T}_G), \boldsymbol{T}_R = \boldsymbol{T}_R(\boldsymbol{\omega}). \tag{3.7}$$

Figure 3.1 provides the daily calculated rotation vector elements and shows them in relation to the observed data, which was gathered over the span of a decade. The given series of z-components are reduced by the arithmetic mean of the observations for readability reasons and are characterised by a negative offset to the observed vector. The other two components show different behaviour than their measured references. The approximation of the first year is as expected, but with further progress, differences and errors increase in relation to the observed rotation vector. In 2006 the simulation approaches the observed data again after the occurring beat. However, by the end of 2010, the simulation is shifting its phase.

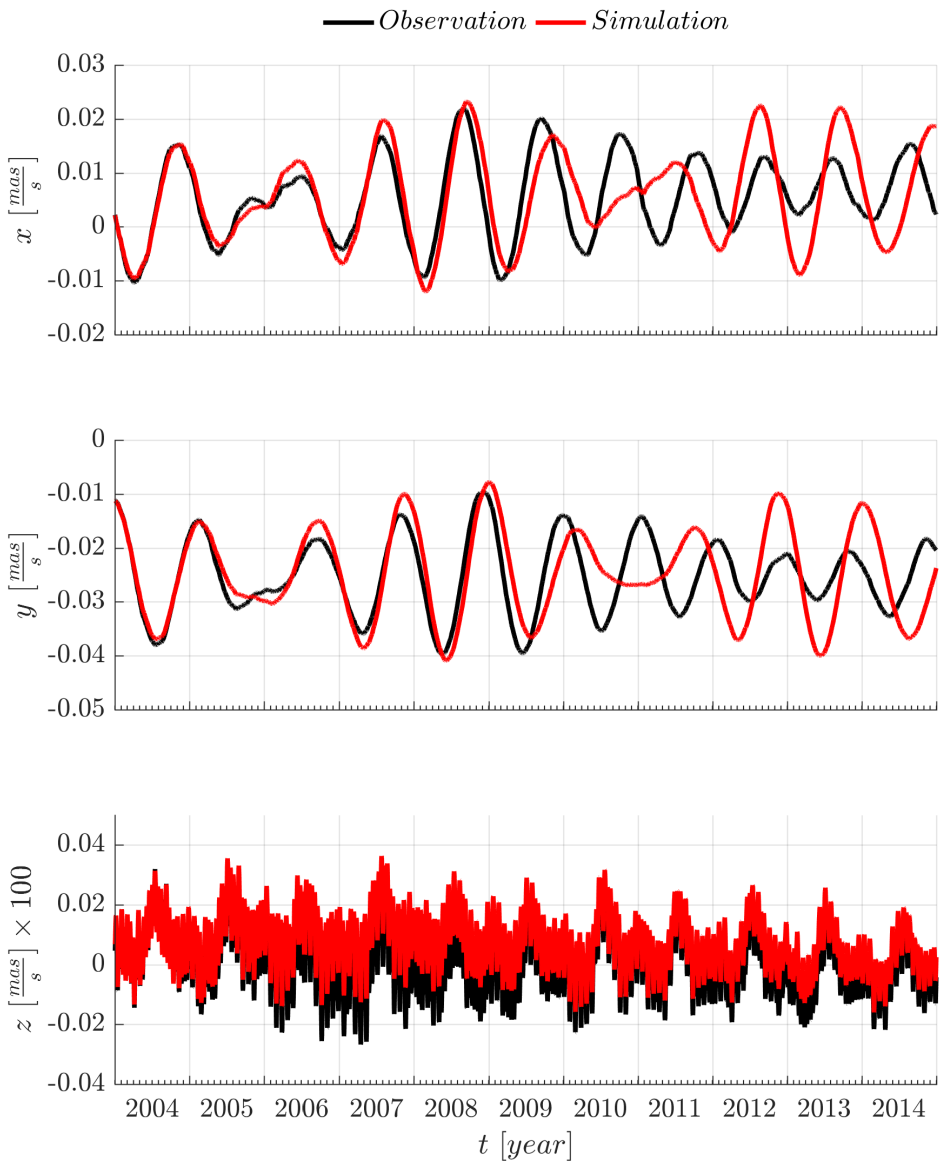

Figure 3.1: Simulated rotation vector in relation to provided observations for the analysed period of 2004 to 2014. Data series of the z-components reduced by arithmetic mean of observations.

4 Adjustment

This chapter focuses on the monthly estimation of spherical harmonic coefficients, the verification of the adjustment and with it the selection of differential values regarding the numerical derivation.
Firstly an overview of the Gauss-Markov Model (Koch, 1999, p. 153f.) is provided and adapted to this thesis' equation and parameters. Furthermore, the necessary linearisation is implemented to adjust the model to the nonlinear equation, which was executed as a numerical as numerical derivation by differences to modified simulated Earth rotation vectors.

4.1 Least square adjustment

An overdetermined system is defined by a majority of observations $\boldsymbol{y}$ with the effect that more equations of observations than unknown parameters $\boldsymbol{x}$ are available. The theoretical background is to find the Best Linear Unbiased Estimator (BLUE) by minimising the squares of residues:

$$\|\boldsymbol{r}\|^2 = \|\boldsymbol{y} - f(\boldsymbol{x})\|^2 \rightarrow min. \tag{4.1}$$

Observations and parameters are both vectors. The relation of these is described by a function $f()$ and can be displayed in a matrix-vector notation. Therefore the $n \times m$ - matrix $\boldsymbol{A}$ is used and is hereafter be referred to as design matrix:

$$\boldsymbol{y} = \boldsymbol{A}\boldsymbol{x} + \boldsymbol{r}. \tag{4.2}$$

The functional interrelation is adapted for the residues to:

$$\|\boldsymbol{r}\|^2 = \|\boldsymbol{y} - \boldsymbol{A}\boldsymbol{x}\|^2 \rightarrow min. \tag{4.3}$$

Each observation is weighted by its reciprocal squared variance, as elements of the diagonal matrix $\boldsymbol{P}$, since correlations between the observations were not considered here. Introducing the weight matrix and substituting the residues leads to:

$$\begin{aligned} \|\boldsymbol{r}\|^2 &= \boldsymbol{r}^T \boldsymbol{P} \boldsymbol{r} \\ &= (\boldsymbol{y} - \boldsymbol{A}\boldsymbol{x})^T \boldsymbol{P} (\boldsymbol{y} - \boldsymbol{A}\boldsymbol{x}) \\ &= \boldsymbol{y}^T \boldsymbol{P} \boldsymbol{y} - 2\boldsymbol{y}^T \boldsymbol{P} \boldsymbol{A} \boldsymbol{x} + \boldsymbol{x}^T \boldsymbol{A}^T \boldsymbol{P} \boldsymbol{A} \boldsymbol{x}. \end{aligned} \tag{4.4}$$

Whereas $\boldsymbol{P}$ is a $n \times n$ - matrix with the number of observations n. In order to ensure the condition of Eq. (4.3) the partial derivations of the square sum of residues are set zero

$$\frac{\delta \|\boldsymbol{r}\|^2}{\delta \boldsymbol{x}} = \boldsymbol{0}. \tag{4.5}$$

Substituting Eq. (4.5) by (4.4) results in the following formula:

$$\begin{aligned} \boldsymbol{0} &= \frac{\delta \left(\boldsymbol{y}^T \boldsymbol{P} \boldsymbol{y} - 2\boldsymbol{y}^T \boldsymbol{P} \boldsymbol{A} \boldsymbol{x} + \boldsymbol{x}^T \boldsymbol{A}^T \boldsymbol{P} \boldsymbol{A} \boldsymbol{x} \right)}{\delta \boldsymbol{x}} \\ &= -2\boldsymbol{y}^T \boldsymbol{P} \boldsymbol{A} + 2\boldsymbol{x}^T \boldsymbol{A}^T \boldsymbol{P} \boldsymbol{A} \\ \boldsymbol{y}^T \boldsymbol{P} \boldsymbol{A} &= \boldsymbol{x}^T \boldsymbol{A}^T \boldsymbol{P} \boldsymbol{A} \\ \boldsymbol{A}^T \boldsymbol{P} \boldsymbol{y} &= \boldsymbol{A}^T \boldsymbol{P} \boldsymbol{A} \boldsymbol{x}. \end{aligned} \tag{4.6}$$

What remains is the final equation to estimate the unknown parameters:

$$\hat{\boldsymbol{x}} = \left(\boldsymbol{A}^T \boldsymbol{P} \boldsymbol{A} \right)^{-1} \boldsymbol{A}^T \boldsymbol{P} \boldsymbol{y}. \tag{4.7}$$

As the adjustment for a linear observation equation is demonstrated, a non-linear model has to be linearised by using approximated values $\boldsymbol{x}_0$ in order to estimate increments of the unknown parameters. Accordingly, the equation of observations is approximated by a Taylor series expansion up to the first derivation term:

$$f(\boldsymbol{x}) \approx f(\boldsymbol{x}_0) + \left. \frac{\delta f(\boldsymbol{x})}{\delta \boldsymbol{x}} \right|_{\boldsymbol{x}_0} (\boldsymbol{x} - \boldsymbol{x}_0). \tag{4.8}$$

Therefore the linearised observation calculates the differences of observations:

$$\Delta \boldsymbol{y} = \boldsymbol{A} \Delta \boldsymbol{x} + \boldsymbol{r}, \tag{4.9}$$

The differences of unknown parameters $\Delta\boldsymbol{x}$, observations $\Delta\boldsymbol{y}$ and the design matrix are computed with the use of the approximated values:

$$\begin{aligned} \Delta\boldsymbol{x} &= \boldsymbol{x} - \boldsymbol{x}_0, \\ \Delta\boldsymbol{y} &= \boldsymbol{y} - f(\boldsymbol{x}_0), \\ \boldsymbol{A} &= \left.\frac{\delta f(\boldsymbol{x})}{\delta \boldsymbol{x}}\right|_{\boldsymbol{x}_0}. \end{aligned} \tag{4.10}$$

The estimation of the parameters is defined analogue to Eq. (4.7) with the linearised design matrix:

$$\Delta\hat{\boldsymbol{x}} = \left(\boldsymbol{A}^T\boldsymbol{P}\boldsymbol{A}\right)^{-1}\boldsymbol{A}^T\boldsymbol{P}\Delta\boldsymbol{y}. \tag{4.11}$$

The corresponding variances of the estimated parameters are determined by the inverted normal equation $\boldsymbol{N}$ and posterior variance $\hat{\sigma}_0^2$:

$$\boldsymbol{\Sigma}\left(\Delta\hat{\boldsymbol{x}}\right) = \hat{\sigma}_0^2\boldsymbol{N}^{-1}, \tag{4.12}$$

$$\text{with } \boldsymbol{N} = \left(\boldsymbol{A}^T\boldsymbol{P}\boldsymbol{A}\right)^{-1}. \tag{4.13}$$

The estimated residues $\hat{\boldsymbol{r}}$ are calculated by the differences of the observations and estimated observations in relation to the degree of freedom within the adjustment – by the numbers of observations n and unknown parameters m

$$\hat{\boldsymbol{r}} = \boldsymbol{y} - \boldsymbol{A}\hat{\boldsymbol{x}}, \tag{4.14}$$

$$\hat{\sigma}_0^2 = \frac{\hat{\boldsymbol{r}}^T\hat{\boldsymbol{r}}}{n-m}. \tag{4.15}$$

4.2 Observation equation and its parameters

Analogue to the general Gauss-Markov model the following differential parameters were introduced to the linear adjustment:

$$\Delta\hat{\boldsymbol{x}} = \begin{bmatrix}\Delta\boldsymbol{\omega_0} & \Delta c_{20} & \Delta c_{21} & \Delta s_{21} & \Delta c_{22} & \Delta s_{22} & \Delta k^{Re} & \Delta k^{Im}\end{bmatrix}^T. \tag{4.16}$$

The first one regarded the starting values ω_0^x, ω_0^y and ω_0^z and covered the uncertainties of the initial values at the numerical integration. Objectives were Δc as well as Δs – representing the differential increments of the respected spherical harmonics cosine and sine coefficients. Real k^{Re} and imaginary part k^{Im} of the Love number permitted variations of these. Adding the increments to the approximated values resulted in the estimated parameters

$$\hat{\boldsymbol{x}} = \Delta\hat{\boldsymbol{x}} - \boldsymbol{x}_0. \tag{4.17}$$

As a result of the Euler-Liouville integration, the simulated vector served as an approximated value $\boldsymbol{y}_0$. The Earth rotation vectors were arranged chronologically, as for the following differential observation vector

$$\Delta\boldsymbol{y} = \begin{pmatrix} \Delta\omega_x(t=1) \\ \Delta\omega_y(t=1) \\ \Delta\omega_z(t=1) \\ \Delta\omega_x(t=2) \\ \Delta\omega_y(t=2) \\ \Delta\omega_z(t=2) \\ \vdots \\ \Delta\omega_x(t=n) \\ \Delta\omega_y(t=n) \\ \Delta\omega_z(t=n) \end{pmatrix}. \tag{4.18}$$

This structure had to utilised as an element order of the design matrix and was necessary for the approach of matrix-vector multiplications. The design matrix was split into the following equations to provide a better representation of its elements concerning the parameters. Attaching the individual matrices $\boldsymbol{A}_{\omega_0}$, $\boldsymbol{A}_{shc}$ and $\boldsymbol{A}_k$ per column leads to the full design matrix:

$$\boldsymbol{A} = \begin{bmatrix} \boldsymbol{A}_{\omega_0} & \boldsymbol{A}_{shc} & \boldsymbol{A}_k \end{bmatrix}. \tag{4.19}$$

$$\boldsymbol{A}_{\omega_0} = \begin{pmatrix} \frac{\delta\omega_x(t=1)}{\delta\omega_0^x} & \frac{\delta\omega_x(t=1)}{\delta\omega_0^y} & \frac{\delta\omega_x(t=1)}{\delta\omega_0^z} \\ \frac{\delta\omega_y(t=1)}{\delta\omega_0^x} & \frac{\delta\omega_y(t=1)}{\delta\omega_0^y} & \frac{\delta\omega_y(t=1)}{\delta\omega_0^z} \\ \frac{\delta\omega_z(t=1)}{\delta\omega_0^x} & \frac{\delta\omega_z(t=1)}{\delta\omega_0^y} & \frac{\delta\omega_z(t=1)}{\delta\omega_0^z} \\ \frac{\delta\omega_x(t=2)}{\delta\omega_0^x} & \frac{\delta\omega_x(t=2)}{\delta\omega_0^y} & \frac{\delta\omega_x(t=2)}{\delta\omega_0^z} \\ \vdots & \vdots & \vdots \\ \frac{\delta\omega_y(t=n)}{\delta\omega_0^x} & \frac{\delta\omega_y(t=n)}{\delta\omega_0^y} & \frac{\delta\omega_y(t=n)}{\delta\omega_0^z} \\ \frac{\delta\omega_z(t=n)}{\delta\omega_0^x} & \frac{\delta\omega_z(t=n)}{\delta\omega_0^y} & \frac{\delta\omega_z(t=n)}{\delta\omega_0^z} \end{pmatrix} \tag{4.20}$$

$$\boldsymbol{A}_{shc} = \begin{pmatrix} \frac{\delta\omega_x(t=1)}{\delta c_{20}} & \frac{\delta\omega_x(t=1)}{\delta c_{21}} & \frac{\delta\omega_x(t=1)}{\delta s_{21}} & \frac{\delta\omega_x(t=1)}{\delta c_{22}} & \frac{\delta\omega_x(t=1)}{\delta s_{22}} \\ \frac{\delta\omega_y(t=1)}{\delta c_{20}} & \frac{\delta\omega_y(t=1)}{\delta c_{21}} & \frac{\delta\omega_y(t=1)}{\delta s_{21}} & \frac{\delta\omega_y(t=1)}{\delta c_{22}} & \frac{\delta\omega_y(t=1)}{\delta s_{22}} \\ \frac{\delta\omega_z(t=1)}{\delta c_{20}} & \frac{\delta\omega_z(t=1)}{\delta c_{21}} & \frac{\delta\omega_z(t=1)}{\delta s_{21}} & \frac{\delta\omega_z(t=1)}{\delta c_{22}} & \frac{\delta\omega_z(t=1)}{\delta s_{22}} \\ \frac{\delta\omega_x(t=2)}{\delta c_{20}} & \frac{\delta\omega_x(t=2)}{\delta c_{21}} & \frac{\delta\omega_x(t=2)}{\delta s_{21}} & \frac{\delta\omega_x(t=2)}{\delta c_{22}} & \frac{\delta\omega_x(t=2)}{\delta s_{22}} \\ \vdots & \vdots & \vdots & \vdots & \vdots \\ \frac{\delta\omega_y(t=n)}{\delta c_{20}} & \frac{\delta\omega_y(t=n)}{\delta c_{21}} & \frac{\delta\omega_y(t=n)}{\delta s_{21}} & \frac{\delta\omega_y(t=n)}{\delta c_{22}} & \frac{\delta\omega_y(t=n)}{\delta s_{22}} \\ \frac{\delta\omega_z(t=n)}{\delta c_{20}} & \frac{\delta\omega_z(t=n)}{\delta c_{21}} & \frac{\delta\omega_z(t=n)}{\delta s_{21}} & \frac{\delta\omega_z(t=n)}{\delta c_{22}} & \frac{\delta\omega_z(t=n)}{\delta s_{22}} \end{pmatrix} \tag{4.21}$$

$$\boldsymbol{A}_k = \begin{pmatrix} \frac{\delta\omega_x(t=1)}{\delta k^{Re}} & \frac{\delta\omega_x(t=1)}{\delta k^{Im}} \\ \frac{\delta\omega_y(t=1)}{\delta k^{Re}} & \frac{\delta\omega_y(t=1)}{\delta k^{Im}} \\ \frac{\delta\omega_z(t=1)}{\delta k^{Re}} & \frac{\delta\omega_z(t=1)}{\delta k^{Im}} \\ \frac{\delta\omega_x(t=2)}{\delta k^{Re}} & \frac{\delta\omega_x(t=2)}{\delta k^{Im}} \\ \vdots & \vdots \\ \frac{\delta\omega_y(t=n)}{\delta k^{Re}} & \frac{\delta\omega_y(t=n)}{\delta k^{Im}} \\ \frac{\delta\omega_z(t=n)}{\delta k^{Re}} & \frac{\delta\omega_z(t=n)}{\delta k^{Im}} \end{pmatrix} \tag{4.22}$$

4.3 Numerical derivation

The functional relation between the observations and parameters was analytically unspecified. Therefore the approach of numerical derivation was applied by modelling the impact of differential variations of the parameters. These characteristics were determined by modifying the parameters of the simulation and the weighted difference to the first simulation:

$$\frac{\delta\boldsymbol{\omega}(t)}{\delta x_i} = \frac{\boldsymbol{\omega}(t) - \boldsymbol{\omega}^i(t)}{\Delta p_i}. \tag{4.23}$$

Where Δp_i states the differential value that was also applied at the modified simulation to its derived parameter. The parameters are indicated by $i = 1 \dots m$ and should, in theory, be as small as possible. A closer review of the resulting number suggested testing each parameter value by itself and in combination with each other for scientific justification. The adapted design matrix $\boldsymbol{A}$ leads to:

$$\boldsymbol{A} \approx \begin{pmatrix} \frac{\boldsymbol{\omega}(1)-\boldsymbol{\omega}^{\omega_0^x}(1)}{\Delta p_{\omega_0^x}} & \frac{\boldsymbol{\omega}(2)-\boldsymbol{\omega}^{\omega_0^x}(2)}{\Delta p_{\omega_0^x}} & \cdots & \frac{\boldsymbol{\omega}(n)-\boldsymbol{\omega}^{\omega_0^x}(n)}{\Delta p_{\omega_0^x}} \\ \frac{\boldsymbol{\omega}(1)-\boldsymbol{\omega}^{\omega_0^y}(1)}{\Delta p_{\omega_0^y}} & \frac{\boldsymbol{\omega}(2)-\boldsymbol{\omega}^{\omega_0^y}(2)}{\Delta p_{\omega_0^y}} & \cdots & \frac{\boldsymbol{\omega}(n)-\boldsymbol{\omega}^{\omega_0^y}(n)}{\Delta p_{\omega_0^y}} \\ \frac{\boldsymbol{\omega}(1)-\boldsymbol{\omega}^{\omega_0^z}(1)}{\Delta p_{\omega_0^z}} & \frac{\boldsymbol{\omega}(2)-\boldsymbol{\omega}^{\omega_0^z}(2)}{\Delta p_{\omega_0^z}} & \cdots & \frac{\boldsymbol{\omega}(n)-\boldsymbol{\omega}^{\omega_0^z}(n)}{\Delta p_{\omega_0^z}} \\ \frac{\boldsymbol{\omega}(1)-\boldsymbol{\omega}^{c_{20}}(1)}{\Delta p_{c_{20}}} & \frac{\boldsymbol{\omega}(2)-\boldsymbol{\omega}^{c_{20}}(2)}{\Delta p_{c_{20}}} & \cdots & \frac{\boldsymbol{\omega}(n)-\boldsymbol{\omega}^{c_{20}}(n)}{\Delta p_{c_{20}}} \\ \frac{\boldsymbol{\omega}(1)-\boldsymbol{\omega}^{c_{21}}(1)}{\Delta p_{c_{21}}} & \frac{\boldsymbol{\omega}(2)-\boldsymbol{\omega}^{c_{21}}(2)}{\Delta p_{c_{21}}} & \cdots & \frac{\boldsymbol{\omega}(n)-\boldsymbol{\omega}^{c_{21}}(n)}{\Delta p_{c_{21}}} \\ \frac{\boldsymbol{\omega}(1)-\boldsymbol{\omega}^{s_{21}}(1)}{\Delta p_{s_{21}}} & \frac{\boldsymbol{\omega}(2)-\boldsymbol{\omega}^{s_{21}}(2)}{\Delta p_{s_{21}}} & \cdots & \frac{\boldsymbol{\omega}(n)-\boldsymbol{\omega}^{s_{21}}(n)}{\Delta p_{s_{21}}} \\ \frac{\boldsymbol{\omega}(1)-\boldsymbol{\omega}^{c_{22}}(1)}{\Delta p_{c_{22}}} & \frac{\boldsymbol{\omega}(2)-\boldsymbol{\omega}^{c_{22}}(2)}{\Delta p_{c_{22}}} & \cdots & \frac{\boldsymbol{\omega}(n)-\boldsymbol{\omega}^{c_{22}}(n)}{\Delta p_{c_{22}}} \\ \frac{\boldsymbol{\omega}(1)-\boldsymbol{\omega}^{s_{22}}(1)}{\Delta p_{s_{22}}} & \frac{\boldsymbol{\omega}(2)-\boldsymbol{\omega}^{s_{22}}(2)}{\Delta p_{s_{22}}} & \cdots & \frac{\boldsymbol{\omega}(n)-\boldsymbol{\omega}^{s_{22}}(n)}{\Delta p_{s_{22}}} \\ \frac{\boldsymbol{\omega}(1)-\boldsymbol{\omega}^{k^{Re}}(1)}{\Delta p_{k^{Re}}} & \frac{\boldsymbol{\omega}(2)-\boldsymbol{\omega}^{k^{Re}}(2)}{\Delta p_{k^{Re}}} & \cdots & \frac{\boldsymbol{\omega}(n)-\boldsymbol{\omega}^{k^{Re}}(n)}{\Delta p_{k^{Re}}} \\ \frac{\boldsymbol{\omega}(1)-\boldsymbol{\omega}^{k^{Im}}(1)}{\Delta p_{k^{Im}}} & \frac{\boldsymbol{\omega}(2)-\boldsymbol{\omega}^{k^{Im}}(2)}{\Delta p_{k^{Im}}} & \cdots & \frac{\boldsymbol{\omega}(n)-\boldsymbol{\omega}^{k^{Im}}(n)}{\Delta p_{k^{Im}}} \end{pmatrix}^T . \quad (4.24)$$

Generating the inverse of the normal equation matrix in Eq. (4.7) may appear numerically critical due to the varying orders of magnitude of matrix elements. Incorrectly scaled elements led to a bad condition of the matrix. An internal system function provided information about the sensitivity of the inverse matrix concerning input changes and round off errors. The function ascertains the ratio of the singular values by singular value decomposition, further described at MATLAB documentation (The MathWorks, 2019, CONDition number for inversion function COND). Therefore a scaling factor was determined of each column to its maximum. Those were applied to the numerical derived elements

to improve the overall ratio of the matrix. Later, the results were reduced by their related scaling values.

4.4 Coefficient estimation per month

The estimation was adjusted to determine coefficients for each month, to agree with standard solutions of reference coefficients such as one of SLR observations. This modification increased the number of coefficient parameters twelve times per year as well as the processing power since the simulated rotation vector was integrated for each month and parameter. The implementation was ordered by parameter type at first and chronologically at second. The months of spherical harmonic coefficients are stated as $t = 1 \dots 132$, between the year 2004 and 2014. The section regarding the coefficient c_{20} increments of the parameter vector is:

$$\Delta\hat{x} = \begin{bmatrix} \cdots & \Delta c_{20}^{1} & \Delta c_{20}^{2} & \cdots & \Delta c_{20}^{t-1} & \Delta c_{20}^{t} & \cdots \end{bmatrix}^{T}. \tag{4.25}$$

The number of parameters expanded from $m = 10$ (Eq. (4.16)) to $m = 665$, by determining all second degree coefficients besides the unique parameters of $\boldsymbol{k}$ and $\boldsymbol{\omega}_0$. Adapting the numerical derived design matrix of spherical harmonic coefficients to temporal resolution of each month leads to:

$$\boldsymbol{A}_{shc} = \begin{pmatrix} \dfrac{\boldsymbol{\omega}(1) - \boldsymbol{\omega}^{c_{20}^{1}}(1)}{\Delta p_{c_{20}^{1}}} & \cdots & \dfrac{\boldsymbol{\omega}(1) - \boldsymbol{\omega}^{c_{20}^{t}}(1)}{\Delta p_{c_{20}^{t}}} & \cdots & \dfrac{\boldsymbol{\omega}(1) - \boldsymbol{\omega}^{s_{22}^{t}}(1)}{\Delta p_{s_{22}^{t}}} \\ \dfrac{\boldsymbol{\omega}(2) - \boldsymbol{\omega}^{c_{20}^{1}}(2)}{\Delta p_{c_{20}^{1}}} & \cdots & \dfrac{\boldsymbol{\omega}(2) - \boldsymbol{\omega}^{c_{20}^{t}}(2)}{\Delta p_{c_{20}^{t}}} & \cdots & \dfrac{\boldsymbol{\omega}(2) - \boldsymbol{\omega}^{s_{22}^{t}}(2)}{\Delta p_{s_{22}^{t}}} \\ \vdots & \ddots & \vdots & \ddots & \vdots \\ \dfrac{\boldsymbol{\omega}(t) - \boldsymbol{\omega}^{c_{20}^{1}}(t)}{\Delta p_{c_{20}^{1}}} & \cdots & \dfrac{\boldsymbol{\omega}(t) - \boldsymbol{\omega}^{c_{20}^{t}}(t)}{\Delta p_{c_{20}^{t}}} & \cdots & \dfrac{\boldsymbol{\omega}(t) - \boldsymbol{\omega}^{s_{22}^{t}}(t)}{\Delta p_{s_{22}^{t}}} \end{pmatrix}. \tag{4.26}$$

An individual number of days d was thereby considered for each month, a one-hour sampling rate as well as leap years, led to $d{\times}24{\times}3 = l$ elements. Simplifying

the notation defines the rotation vectors per month t and parameters i:

$$\boldsymbol{\omega}(t) = \begin{pmatrix} \omega_x(1) \\ \omega_y(1) \\ \omega_z(1) \\ \omega_x(2) \\ \omega_y(2) \\ \omega_z(2) \\ \vdots \\ \omega_x(l) \\ \omega_y(l) \\ \omega_z(l) \end{pmatrix}, \; \boldsymbol{\omega}^{i^t}(t) = \begin{pmatrix} \omega_x^{i^t}(1) \\ \omega_y^{i^t}(1) \\ \omega_z^{i^t}(1) \\ \omega_x^{i^t}(2) \\ \omega_y^{i^t}(2) \\ \omega_z^{i^t}(2) \\ \vdots \\ \omega_x^{i^t}(l) \\ \omega_y^{i^t}(l) \\ \omega_z^{i^t}(l) \end{pmatrix}. \tag{4.27}$$

Differential values altered only elements of the respective months at the numeric integration in the course of computing the numerical derivation. The numerical derived results of the design matrix were zero until the associated month of the coefficient was reached.

$$\boldsymbol{\omega}(j) = \boldsymbol{\omega}^{i^t}(j) \text{ with } j < t \tag{4.28}$$

4.5 Adjustment verification

The correctness of the least square adjustment was proven in a simulation case by modifying its observation vector and approximated parameters. Adjusting these for various approaches established the scientific interpretation and further recognised coherence. Therefore the simulated vector was introduce as the observation vector of the adjustment, leading to differential observation vector equals zero ($\Delta \boldsymbol{y} = \boldsymbol{0}$).
A constant value c was applied to an initial parameter at the process of simulating the rotation vector. The application should further be the estimated increment of the related parameter. Therefore, one or several months were tested. Additionally, the sizes of the constant value, as well as derivation increment, were adjusted, leading to multiple combinations. Each adjustment included the determination of the differential rotation vector components. The derivation

step size of these were predefined as 10^{-12} rad/s, in relation to obtainable accuracies of EOP data by IERS (2013).

Verifying the Love number was realised by modifying each part of the whole decade. Whereby both parts were estimated due to their correlation in addition to the initial vector. The matching digits between the determined increment and used constant value in relation to the step size of numerical derivation is listed in Tab. 4.1.

Table 4.1: Identical digits between estimated increments $\Delta\hat{k^{Re}}$ and test value c of the real Love number in relation to the used numerical derivation interval $\Delta p_{k^{Re}}$.

	Applied value c to k^{Re}			
Interval $\Delta p_{k^{Re}}$	10^{-4}	10^{-5}	10^{-6}	10^{-7}
10^{-4}	10^{-17}	10^{-7}	10^{-8}	10^{-9}
10^{-5}	10^{-6}	10^{-18}	10^{-9}	10^{-10}
10^{-6}	10^{-6}	10^{-8}	10^{-19}	10^{-11}
10^{-7}	10^{-6}	10^{-8}	10^{-10}	10^{-19}

The following cases of the results are thereby distinguished:

- Case one: $\Delta p_i = c$.
- Case two: $\Delta p_i \neq c$.

The principal diagonal of Tab. 4.1 contains the first case, with the remaining elements as a representation of the second case. The differences between the estimations and test value were smaller in the first case. This pattern continued in the acquired accuracies of the covariance matrix, characterized in Fig. 4.1a with modification value and derivation interval equal 10^{-4}. The obtained variances were above 10^{-40} of the first case, in contrast to the second case illustrated in Fig. 4.1b(step size 10^{-6} and constant value 10^{-4}). The estimated parameters were, therefore, more accurate regarding the first case, where the increment size is consistent with derivation one. Elements of the covariance matrices along the principal diagonal are squared, and therefore the square root has to be taken to consider those as accuracies of the parameters.

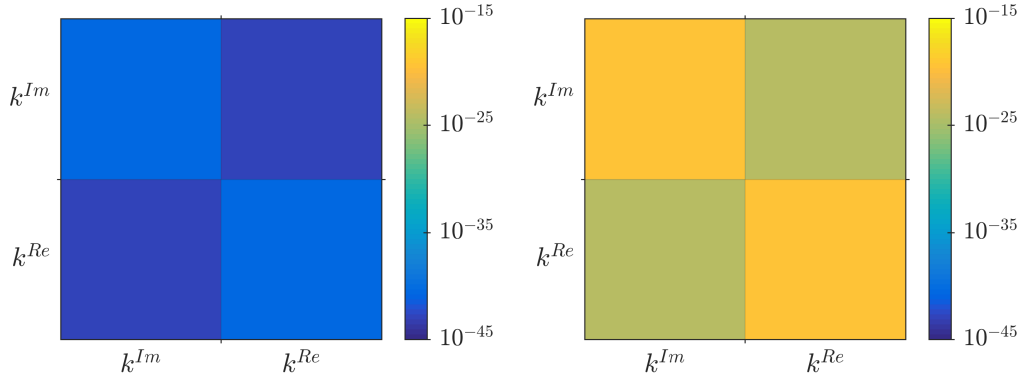

(a) First case (b) Second case

Figure 4.1: Covariance matrix of real part of the Love number k^{Re} computed at the adjustment verification. Two distinguished cases: (a) derivation increment equal test value 10^{-4} and (b) derivation increment 10^{-6} unequal test value 10^{-4}.

The results of the imaginary part were similar and are represented in Tab. 4.2.

Table 4.2: Identical digits between estimated increments $\Delta\hat{k^{Im}}$ and test value c of the imaginary Love number in relation to the used numeric derivation interval $\Delta p_{k^{Im}}$.

	Applied value c to k^{Im}			
Interval $\Delta p_{k^{Im}}$	10^{-4}	10^{-5}	10^{-6}	10^{-7}
10^{-4}	10^{-18}	10^{-7}	10^{-8}	10^{-9}
10^{-5}	10^{-6}	10^{-18}	10^{-9}	10^{-10}
10^{-6}	10^{-6}	10^{-8}	10^{-20}	10^{-11}
10^{-7}	10^{-6}	10^{-8}	10^{-10}	10^{-20}

The correctness of determining the Love number was confirmed since the modified values were adequately estimated. The accuracy of the increments differed depending on the step size of numerical derivation.

Validating the coefficients of spherical harmonics was accomplished by modifying one or several months of its parameter. Figure 4.2 displays approaches of the connection between the derivation interval and applied test value of

different magnitudes. The behaviour was likewise to the Love numbers, and estimated results approved the implementation. The increments are indicated at logarithmic scales along the y-axis. Figures 4.2a and 4.2b show the first case, whereby the numeric derivation equals estimated value. The altered fifth month is obvious. The remaining increments of the parameters were consistent and considered zero, due to the difference to the actual increment. The second row of the figure indicates the second case with Figs. 4.2c and 4.2d. Although the modified month was certainly detectable, the determined values were not as stable as in the first case and settling after the altered month.

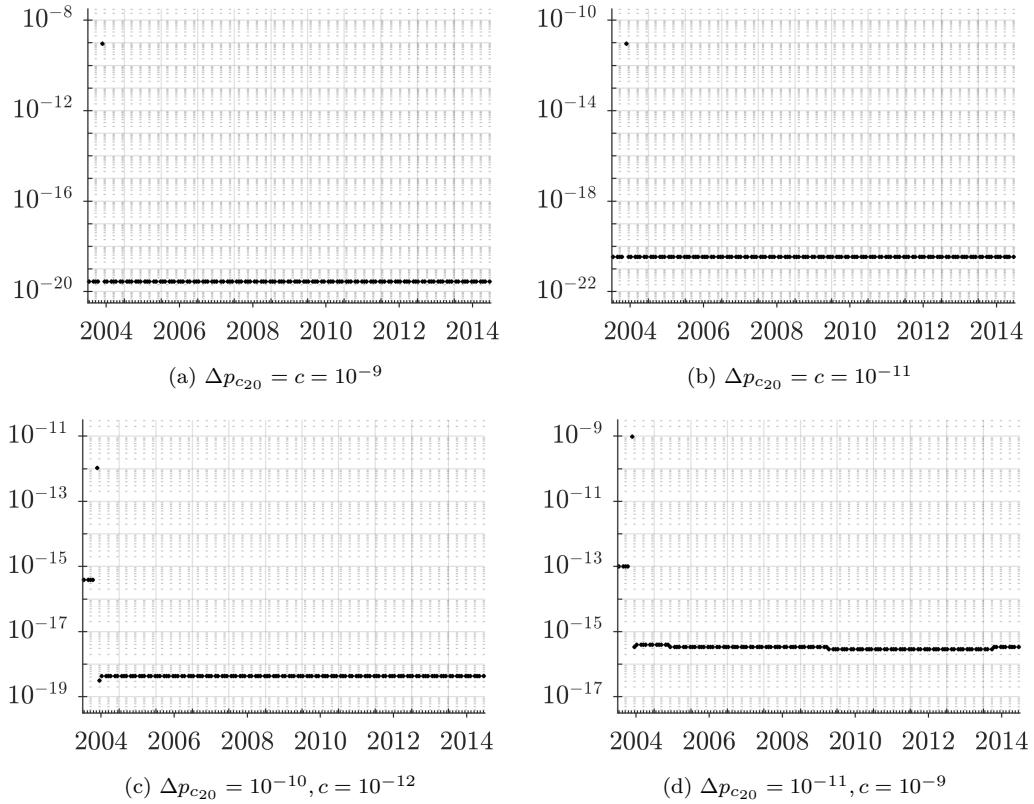

(a) $\Delta p_{c_{20}} = c = 10^{-9}$

(b) $\Delta p_{c_{20}} = c = 10^{-11}$

(c) $\Delta p_{c_{20}} = 10^{-10}, c = 10^{-12}$

(d) $\Delta p_{c_{20}} = 10^{-11}, c = 10^{-9}$

Figure 4.2: Estimated spherical harmonic coefficient increments $\Delta\hat{x}_{c_{20}}$ determined at adjustment verification of one altered month. Estimated parameters were $\Delta\omega_0$ and Δc_{20} for the time period between the years 2004 and 2014. Algorithm adjustments: (a) $\Delta p_{c_{20}} = c = 10^{-9}$, (b) $\Delta p_{c_{20}} = c = 10^{-11}$, (c) $\Delta p_{c_{20}} = 10^{-10}$, $c = 10^{-12}$ and (d) $\Delta p_{c_{20}} = 10^{-11}$, $c = 10^{-9}$.

The achieved coefficient increments of $\Delta\hat{x}_{c_{21}}$ are characterized in Fig. 4.3. A weaker correlation between Δp and c was noticeable of both first order spherical harmonics c_{21} and s_{21} (see Fig. 4.4). This was possible due to the good determinability of the tesseral coefficients.

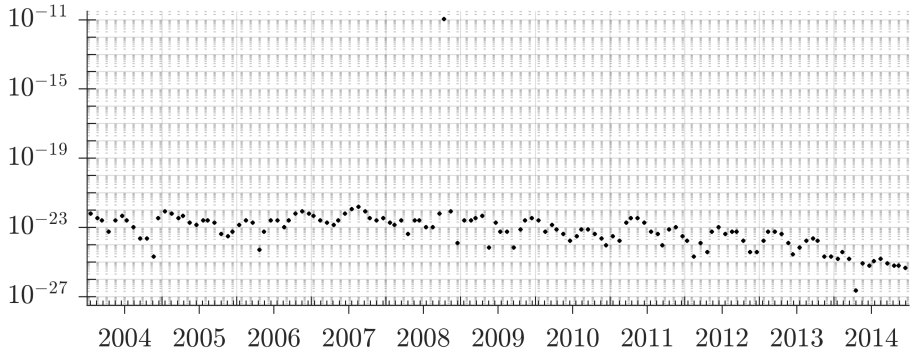

(a) $\Delta p_{c_{21}} = c = 10^{-11}$

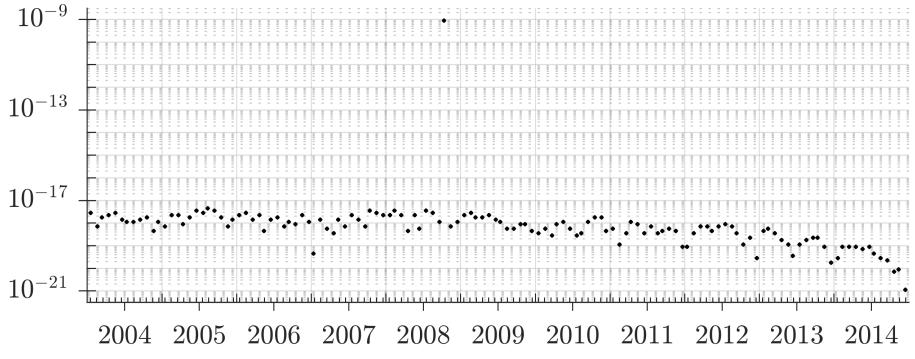

(b) $\Delta p_{c_{21}} = 10^{-12}, c = 10^{-9}$

Figure 4.3: Estimated spherical harmonic coefficient increments $\Delta\hat{x}_{c_{21}}$ determined at adjustment verification of one altered month. Estimated parameters were $\Delta\omega_0$ and Δc_{21} for the time period between the years 2004 and 2014. Algorithm adjustments: (a) $\Delta p_{c_{21}} = c = 10^{-11}$ and (b) $\Delta p_{c_{21}} = 10^{-12}$, $c = 10^{-9}$.

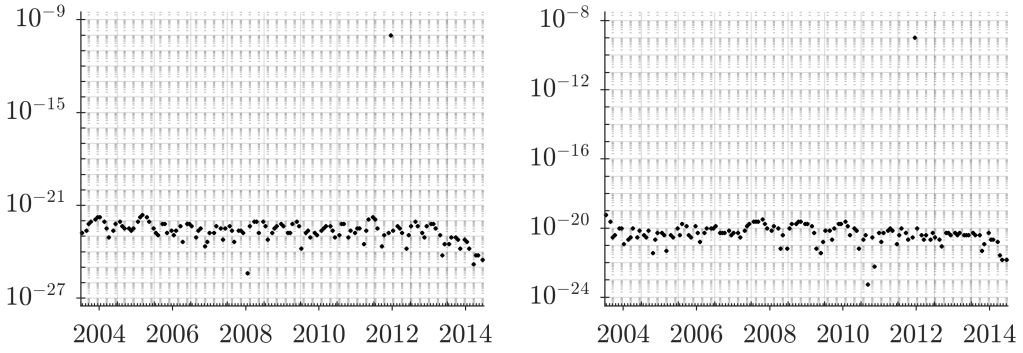

(a) $\Delta p_{s_{21}} = c = 10^{-10}$ (b) $\Delta p_{s_{21}} = 10^{-11}, c = 10^{-9}$

Figure 4.4: Estimated spherical harmonic coefficient increments $\Delta\hat{x}_{s_{21}}$ determined at adjustment verification of one altered month. Estimated parameters were $\Delta\omega_0$ and Δc_{21} for the time period between the years 2004 and 2014. Algorithm adjustments: (a) $\Delta p_{s_{21}} = c = 10^{-10}$ and (b) $\Delta p_{s_{21}} = 10^{-11}$, $c = 10^{-9}$.

Further outcome validating the adjustment are displayed in Figs. 4.5 and 4.5 for remaining second degree coefficients c_{22}, s_{22}.

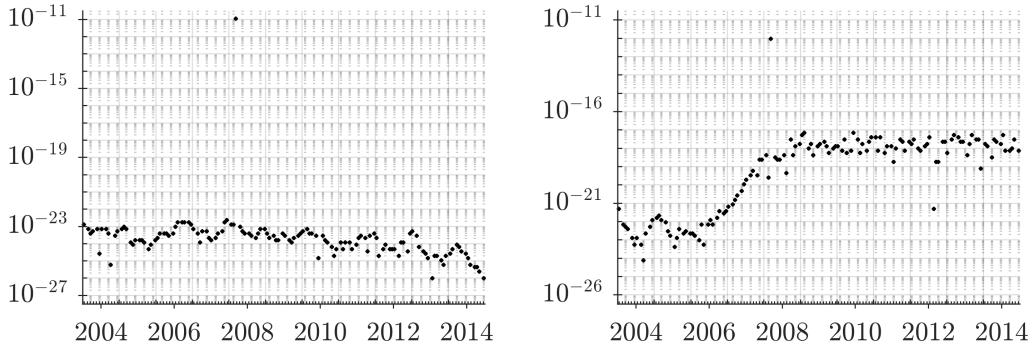

(a) $\Delta p_{c_{22}} = c = 10^{-11}$ (b) $\Delta p_{c_{22}} = 10^{-11}, c = 10^{-12}$

Figure 4.5: Estimated spherical harmonic coefficient increments $\Delta\hat{x}_{c_{22}}$ determined at adjustment verification of one altered month. Estimated parameters were $\Delta\omega_0$ and Δc_{22} for the time period between the years 2004 and 2014. Algorithm adjustments: (a) $\Delta p_{c_{22}} = c = 10^{-11}$ and (b) $\Delta p_{c_{22}} = 10^{-11}$, $c = 10^{-12}$.

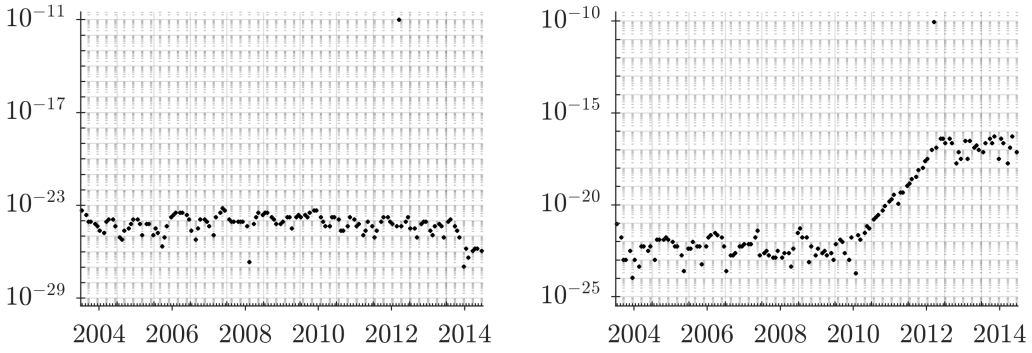

(a) $\Delta p_{s_{22}} = c = 10^{-11}$ (b) $\Delta p_{s_{22}} = 10^{-11}, c = 10^{-10}$

Figure 4.6: Estimated spherical harmonic coefficient increments $\Delta\hat{x}_{s_{22}}$ determined at adjustment verification of one altered month. Estimated parameters were $\Delta\omega_0$ and Δs_{22} for the time period between the years 2004 and 2014. Algorithm adjustments: (a) $\Delta p_{s_{22}} = c = 10^{-11}$ and (b) $\Delta p_{s_{22}} = 10^{-11}$, $c = 10^{-10}$.

The implemented adjustment was considered correct for differences of spherical harmonic coefficients, Love number, and the initial vector. The results of the latter are not explicitly shown since the result did not present further information. However, the selection of the numerical derivation step size seemed essential concerning the estimations. Therefore, the related increment was defined concerning the expected size of the determined parameters. Certainties of Love number parts were not known, and the numeric derivation increment was chosen based on the last provided decimal numbers:

$$\Delta p_{k^{Re}} = \Delta p_{k^{Im}} = 10^{-4}. \tag{4.29}$$

The accuracies of the observation vector y were not specified either, which appeared in the adjustment as well as reciprocal elements of the weighted matrix. Therefore the accuracies were calculated with aid of EOPS data by IERS (2013) and converted using Eqs. (2.6) and (2.8). The accuracies were introduced equally of every component, although the determined accuracies of the axis varied, and the z-axis is, in general, more accurate:

$$\sigma_{\omega_x} = \sigma_{\omega_x} = \sigma_{\omega_x} = \Delta p_{\omega_x} = \Delta p_{\omega_x} = \Delta p_{\omega_x} = 10^{-12}. \tag{4.30}$$

Two solutions were considered for the accuracies of spherical harmonic coefficients. A satellite-only gravity field model from the Gravity Observation COmbination (GOCO) – the GOCO05s (GOCO, 2019)– and the Earth's dynamic oblateness of SLR observations by JPL, 2014b, related to (Cheng et al., 2011). The accuracies from the SLR model were adapted to the derivation increment size:

$$\Delta p_{c_{20}} = \Delta p_{c_{21}} = \Delta p_{s_{21}} = \Delta p_{c_{22}} = \Delta p_{s_{22}} = 10^{-11}. \tag{4.31}$$

5 Estimated parameters

The estimated increments are represented for different combinations of the parameters. Introducing various combinations of the adjustment facilitates the comparison and verifies the parameters that can be best-estimated incoherence to Earth's rotation vector. A solution of SLR observations, obtained from JPL (2014b) (Cheng et al., 2011) served as reference coefficients. The parameters are therefore categorised into each order of the spherical harmonic coefficients, components of the initial vector and parts of the Love number due to the correlation between these parameter types.

The coefficients of the second degree spherical harmonics were the results of determining these parameters for each month in contrary to the initial rotation vector and Love number, which are estimated once for the whole period – for the time frame of January, 1st 2004 to December, 31th 2014. Therefore the predefined accuracies of Sec. 4.5 were used as differentials at the numerical derivation as well as for the uniform weight matrix of the observations.

5.1 Spherical harmonics coefficients

Coefficient c_{20}

The determined coefficient increments of the zonal second degree spherical harmonic c_{20} contained a yet unknown bias. Figure 5.1 illustrates spherical harmonic coefficients including the determined increments, initial (see Sec. 3.1) and reference coefficients. The latter two are reduced by the arithmetic mean of the reference time series. The data sets appear as linear lines without visible oscillations, where the SLR graph is overlaid by the approximated coefficients, due to the constant offset value of 10^{-6} within the estimated increments. The

variations of c_{20} coefficients were expected at the size of the predefined accuracy 10^{-11}.

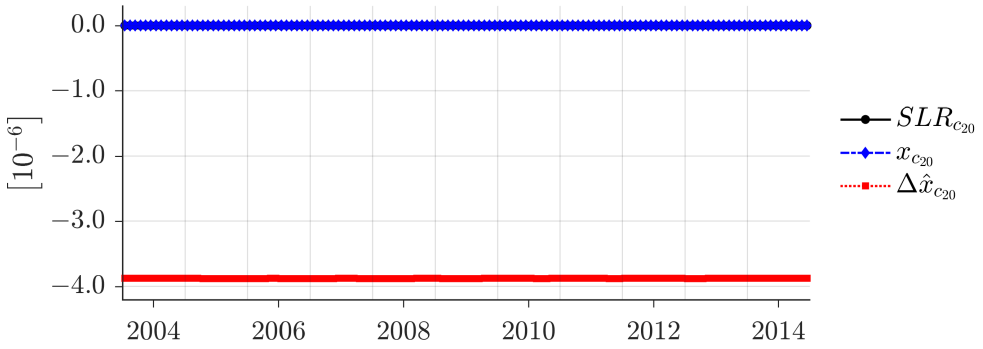

Figure 5.1: Estimated coefficient increments (red dotted line) of the zeroth order $\Delta\hat{\boldsymbol{c}}_{20}$ compared to initial data series of the implemented coefficients (blue dashed line) at the numerical integration of Earth's rotation vector and published reference data of SLR observations (black line). The initial and reference coefficients are reduced by the mean value of SLR data.

The steady trend changed with further determined parameters but still existed in all considered combinations. Figure 5.2 displays the magnitude of the absolute increments of various adjustment versions. The offset did not occur at the validation of the algorithm in Sec. 4.5 or in the increments of other parameters by introducing c_{20} to the adjustment. Therefore, the obtained offsets were most probably based within the initial spherical harmonic data sets. Including the Love number parameters in addition to the zeroth order coefficient, which increased the obtained constant value. The extension by further spherical harmonics coefficients (c_{21}, s_{21} or c_{22}, s_{22}) decreased the bias, whereas the determined accuracy from the covariance matrix decreased as well.

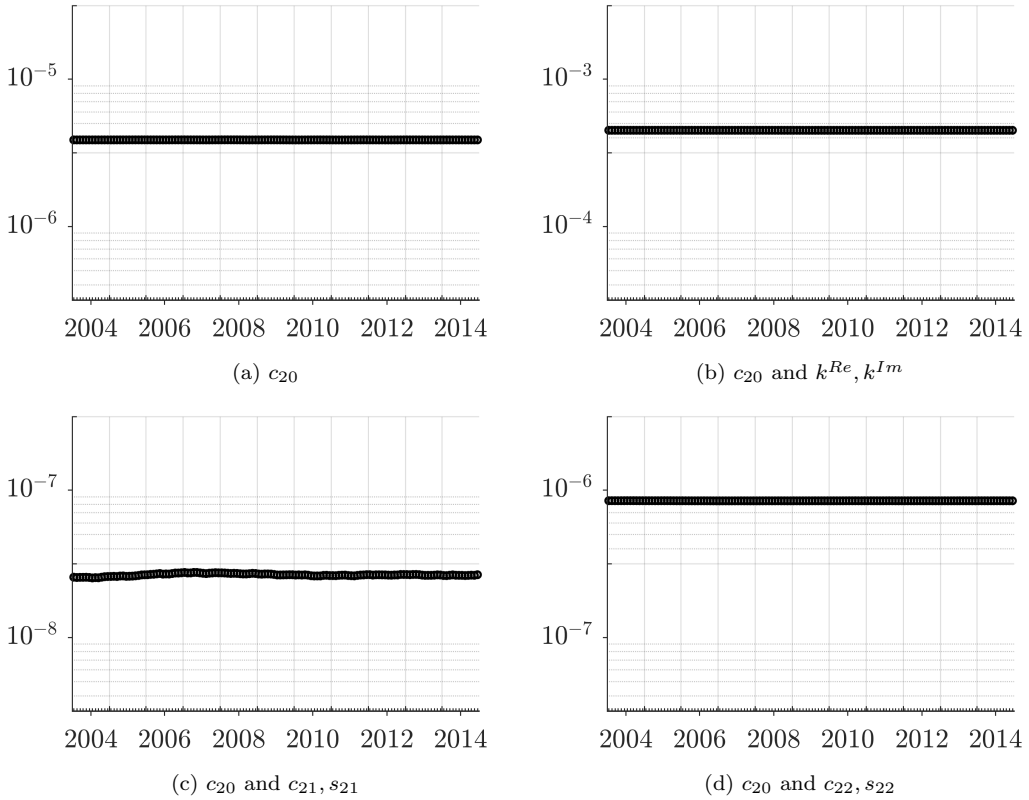

(a) c_{20} (b) c_{20} and k^{Re}, k^{Im}

(c) c_{20} and c_{21}, s_{21} (d) c_{20} and c_{22}, s_{22}

Figure 5.2: Absolute estimated increments of coefficients c_{20} determined by an adjustment including the parameters: (a) -, (b) Love number $\boldsymbol{k}$, (c) first order coefficients c_{21}, s_{21}, (d) second order coefficients c_{22}, s_{22} – besides the initial vector $\boldsymbol{\omega}_0$ and coefficient c_{20}.

Table 5.1 contains the arithmetic mean values, standard derivations of the estimated increments $\Delta\hat{c}_{20}$ and the achieved certainties from the covariance matrix $\hat{\sigma}_{c_{20}}$. The offset is represented by the average μ and appear several exponents larger than the variations of the data series. The second statistical parameter was stable at 10^{-10}, despite the standalone version and further determination of the Love number. However, the obtained accuracies were larger than their oscillations, which indicated a poor determinability of coefficient c_{20} for all combinations.
The highest certainties within the adjustment were achieved by the standalone estimation of the parameter, followed by the combinations with other spherical

harmonic coefficients. The bias of second order coefficients c_{22}, s_{22} combination stood out as the only positive one. The sign changed to negative again by adding the Love number to the adjustment. Other than that, the Love numbers had hardly any influence on the outcome of combinations with multiple spherical harmonic coefficients. Declaring which combination is the most suitable was barely possible, due to the unknown dimension and source of the encountering offset. The extracted certainties of the covariance matrices were expected to fit the estimated increments.

Table 5.1: Statistical parameters of the coefficient increments $\Delta\hat{\boldsymbol{c}}_{20}$ and the obtained certainties $\hat{\sigma}_{c_{20}}$ for implemented parameter combinations.

$\hat{\boldsymbol{x}}\{\boldsymbol{\omega}_0, c_{20}, \dots\}$	$\mu\left(\Delta\hat{\boldsymbol{c}}_{20}\right)$	$s\left(\Delta\hat{\boldsymbol{c}}_{20}\right)$	$\hat{\sigma}_{c_{20}}$
$-$	-3.877×10^{-6}	1.5×10^{-9}	$\pm 2.00 \times 10^{-8}$
$\boldsymbol{k}$	-4.504×10^{-4}	8.7×10^{-8}	$\pm 3.53 \times 10^{-6}$
c_{21}, s_{21}	-1.818×10^{-7}	5.2×10^{-10}	$\pm 2.45 \times 10^{-7}$
c_{22}, s_{22}	8.447×10^{-7}	5.2×10^{-10}	$\pm 2.35 \times 10^{-7}$
$c_{21}, s_{21}, \boldsymbol{k}$	-1.283×10^{-8}	5.1×10^{-10}	$\pm 2.52 \times 10^{-7}$
$c_{21}, s_{21}, c_{22}, s_{22}$	-2.523×10^{-7}	5.2×10^{-10}	$\pm 2.33 \times 10^{-7}$
$c_{21}, s_{21}, c_{22}, s_{22}, \boldsymbol{k}$	-2.664×10^{-8}	5.1×10^{-10}	$\pm 2.32 \times 10^{-7}$
$c_{22}, s_{22}, \boldsymbol{k}$	-1.018×10^{-8}	5.1×10^{-10}	$\pm 2.52 \times 10^{-7}$

Removing the zero degrees trend from the summarised approximated spherical harmonics and estimated increments show the temporal variations in Fig. 5.3. The combinations with additional spherical harmonics coefficients have a similar signal behaviour – contained more high-frequent variations and showed a noticeable different amplitude than the standalone version.

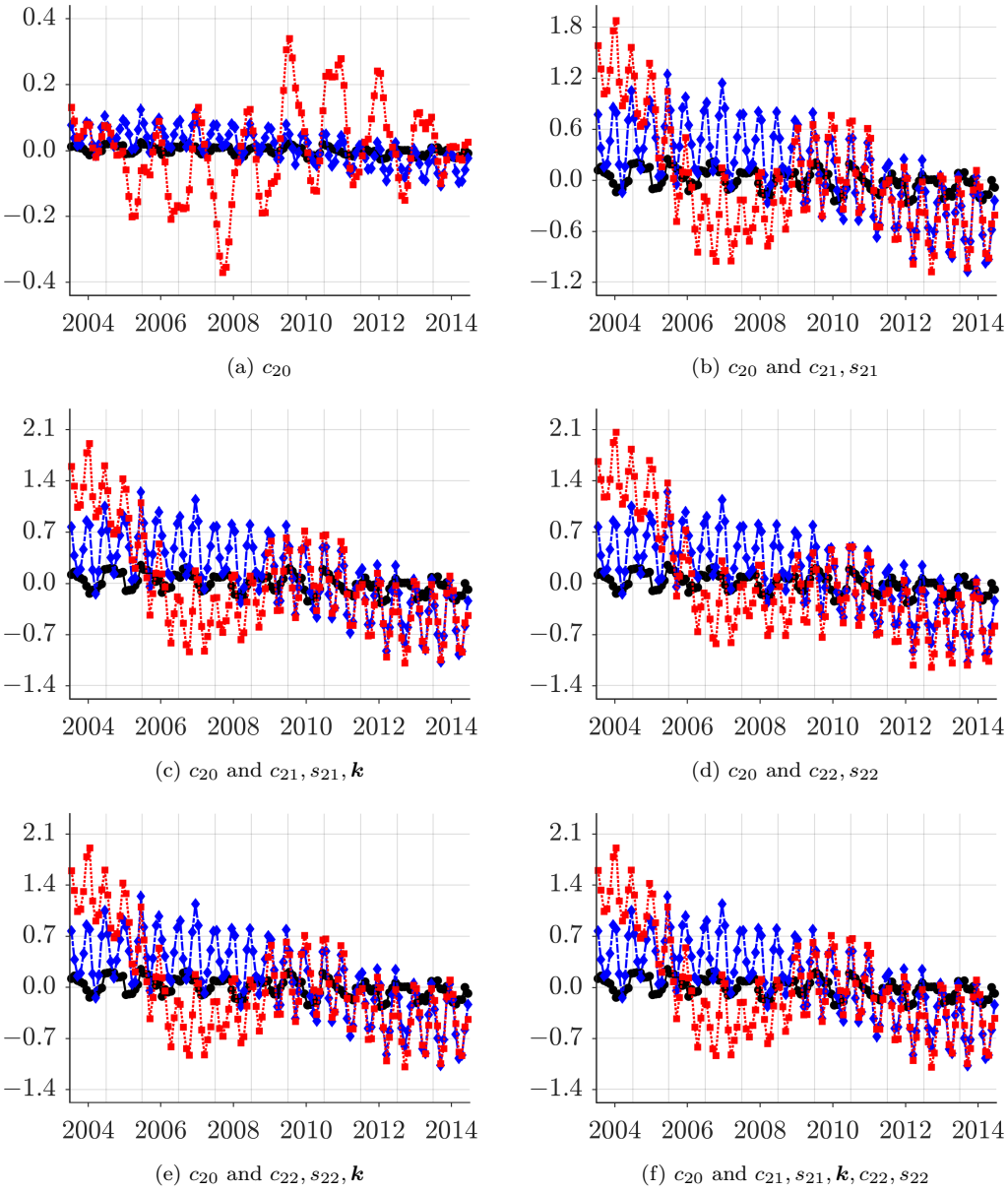

(a) c_{20}

(b) c_{20} and c_{21}, s_{21}

(c) c_{20} and $c_{21}, s_{21}, \boldsymbol{k}$

(d) c_{20} and c_{22}, s_{22}

(e) c_{20} and $c_{22}, s_{22}, \boldsymbol{k}$

(f) c_{20} and $c_{21}, s_{21}, \boldsymbol{k}, c_{22}, s_{22}$

Figure 5.3: Comparison of the spherical harmonics coefficients $c_{20} \times 10^{+9}$. Reference data of SLR observations reduced by arithmetic average (black line). Initial coefficients for the simulation (blue dashed line), see Ch. 3, reduced by the mean value of the reference series. Mean free series of combining the initial coefficients and estimated increments (red dotted line). Determined parameters: (a) -, (b) c_{21} and s_{21}, (c) c_{21}, s_{21} and $\boldsymbol{k}$, (d) c_{22}, s_{22}, (e) c_{22}, s_{22} and $\boldsymbol{k}$, (f) $c_{21}, s_{21}, c_{22}, s_{22}$ and $\boldsymbol{k}$ – besides $c_{20}, \boldsymbol{\omega}_0$.

The divergent results of the Love number combination are displayed in Fig. 5.4. The time series illustrated an oscillation over the whole period, due to the weak coherence of coefficient c_{20} and Love number $\boldsymbol{k}$.

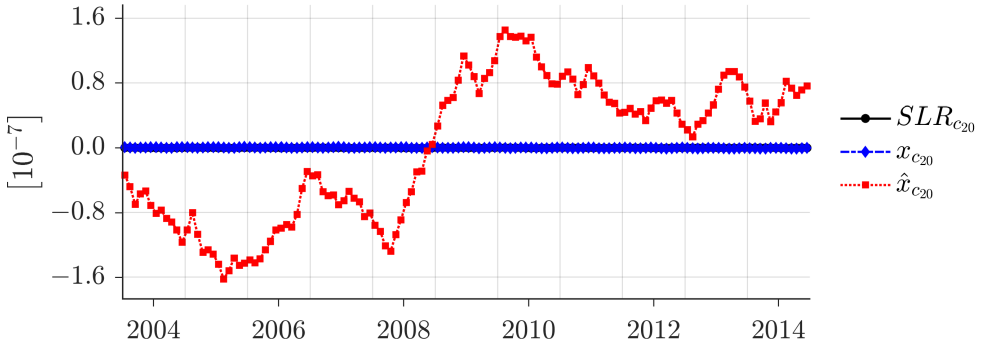

Figure 5.4: Mean free spherical harmonics coefficients $\hat{\boldsymbol{c}}_{20}$ estimated with $\boldsymbol{\omega}_0, c_{20}$ and $\boldsymbol{k}$ (red dotted line). Reference data of SLR observations reduced by its arithmetic average (black line). Initial coefficients of the simulation (blue dashed line), see Ch. 3, reduced by mean value of SLR data.

Coefficients c_{21} and s_{21}

Figure 5.5 illustrates tesseral spherical harmonic coefficients c_{21} and s_{21}. Visualised are the estimated increments, reference coefficients of SLR observations and provided initial coefficients of the simulation. The latter two data sets were reduced by the arithmetic mean of the reference series. Neither of the increment data sets contained a bias as the coefficient increments of c_{20} since the first statistical parameter is in relation close to zero. The static differences between the initial spherical harmonic and reference coefficients were larger than estimated increments values. Therefore, adjusting the initial coefficients by the increments did not lead to a significant improvement to the reference coefficients.

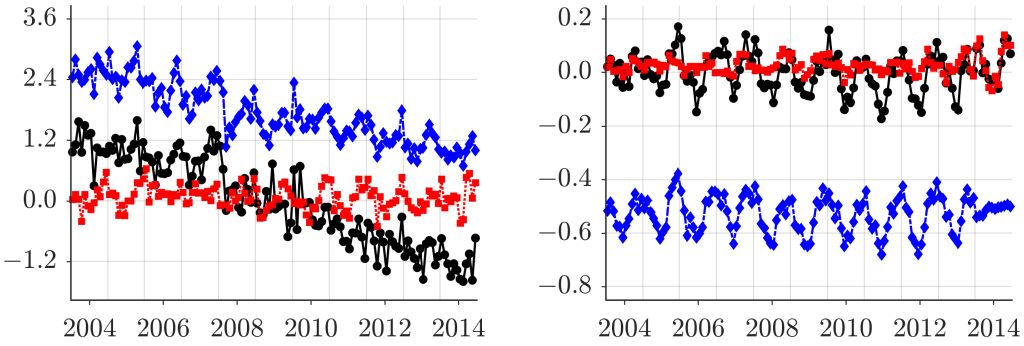

(a) c_{21} (b) s_{21}

Figure 5.5: Estimated coefficient increments (red dotted line) of the first order (a) $\Delta\hat{\boldsymbol{c}}_{21} \times 10^{+10}$ and (b) $\Delta\hat{\boldsymbol{s}}_{21} \times 10^{+9}$ in comparison to the initial coefficients (blue dashed line) for numerical integration of the Earth's rotation vector and published reference data of SLR observations (black line). The initial and reference coefficients were reduced by the arithmetic mean of the reference series.

The outcome of the increments and their obtained variances are listed in Tab. 5.2 regarding $\Delta\hat{\boldsymbol{c}}_{21}$ and Tab. 5.3 concerning $\Delta\hat{\boldsymbol{s}}_{21}$. The achieved information of both spherical harmonic coefficients was analogous, besides the different dimensions and signs of the arithmetic mean of the data. The average of the estimated values was smaller than their standard derivation for both coefficient increments, except two versions of $\Delta\hat{\boldsymbol{c}}_{21}$ that included the Love number and the zonal spherical harmonic coefficient. The standard derivation of the time series increased by adding additional unknown parameters as well as the uncertainties within the adjustment. The best variances were achieved with the standalone versions. The obtained certainties of determining all parameters fitted the predefined certainties of 10^{-11} as well. The stable behaviour and sufficient accuracies lead to the assumption that both tesseral spherical harmonic coefficients are well determinable regarding Earth's rotation vector variations.
The zonal spherical harmonic coefficient c_{20} confirmed no major influence on the estimation of the coefficient increments $\Delta c_{21}, \Delta s_{21}$, displayed in Fig. 5.6. The figure also shows no visible differences for the various parameter combinations. The estimated values were thereby to small to identify neither a positive or negative change of the applied time series.

Table 5.2: Statistical parameters of the coefficient increments $\Delta\hat{\boldsymbol{c}}_{21}$ and the obtained certainties $\hat{\sigma}_{c_{21}}$ for implemented parameter combinations.

$\hat{\boldsymbol{x}}\{\boldsymbol{\omega}_0, c_{21}, s_{21}, \dots\}$	$\mu\,(\Delta\hat{\boldsymbol{c}}_{21})$	$s\,(\Delta\hat{\boldsymbol{c}}_{21})$	$\hat{\sigma}_{c_{21}}$
–	-6.662×10^{-12}	2.3×10^{-11}	$\pm 5.90 \times 10^{-13}$
$\boldsymbol{k}$	-3.868×10^{-11}	2.8×10^{-11}	$\pm 3.24 \times 10^{-12}$
c_{20}	6.546×10^{-12}	2.3×10^{-11}	$\pm 6.39 \times 10^{-13}$
c_{22}, s_{22}	7.491×10^{-11}	6.9×10^{-10}	$\pm 4.07 \times 10^{-11}$
$c_{20}, \boldsymbol{k}$	-3.792×10^{-11}	2.8×10^{-11}	$\pm 3.15 \times 10^{-12}$
c_{20}, c_{22}, s_{22}	8.191×10^{-11}	6.9×10^{-10}	$\pm 3.94 \times 10^{-11}$
$c_{20}, c_{22}, s_{22}, \boldsymbol{k}$	1.692×10^{-10}	8.5×10^{-10}	$\pm 4.99 \times 10^{-11}$
$c_{22}, s_{22}, \boldsymbol{k}$	1.265×10^{-10}	8.3×10^{-10}	$\pm 5.16 \times 10^{-11}$

Table 5.3: Statistical parameters of the coefficient increments $\Delta\hat{\boldsymbol{s}}_{21}$ and the obtained certainties $\hat{\sigma}_{s_{21}}$ for implemented parameter combinations.

$\hat{\boldsymbol{x}}\{\boldsymbol{\omega}_0, c_{21}, s_{21}, \dots\}$	$\mu\,(\Delta\hat{\boldsymbol{s}}_{21})$	$s\,(\Delta\hat{\boldsymbol{s}}_{21})$	$\hat{\sigma}_{s_{21}}$
–	2.485×10^{-11}	3.3×10^{-11}	$\pm 5.90 \times 10^{-13}$
$\boldsymbol{k}$	2.259×10^{-11}	2.9×10^{-11}	$\pm 3.23 \times 10^{-12}$
c_{20}	2.537×10^{-11}	3.3×10^{-11}	$\pm 9.18 \times 10^{-13}$
c_{22}, s_{22}	6.082×10^{-12}	8.4×10^{-10}	$\pm 4.07 \times 10^{-11}$
$c_{20}, \boldsymbol{k}$	2.324×10^{-11}	2.9×10^{-11}	$\pm 3.14 \times 10^{-12}$
c_{20}, c_{22}, s_{22}	8.807×10^{-12}	8.3×10^{-10}	$\pm 3.94 \times 10^{-11}$
$c_{20}, c_{22}, s_{22}, \boldsymbol{k}$	5.004×10^{-10}	9.2×10^{-10}	$\pm 4.99 \times 10^{-11}$
$c_{22}, s_{22}, \boldsymbol{k}$	4.680×10^{-10}	9.1×10^{-10}	$\pm 5.16 \times 10^{-11}$

The Love number parts k^{Re}, k^{Im} as well as sectoral spherical harmonic coefficients c_{22}, s_{22} increased the estimated increments, see Fig. 5.7. Whereby variations of the determined coefficients exceeded the scaling of both external time series oscillations. The major differences at the end of 2005 and 2010 resembled the inconsistency of the simulated earth rotation vector to the observations of Fig. 3.1. Introducing the Love numbers increased the amplitude of $\hat{\boldsymbol{c}}_{21}$, approaching the reference series of SLR observations. No differences were

noticeable for the sinus coefficient of the first order with the same adjustment conditions.

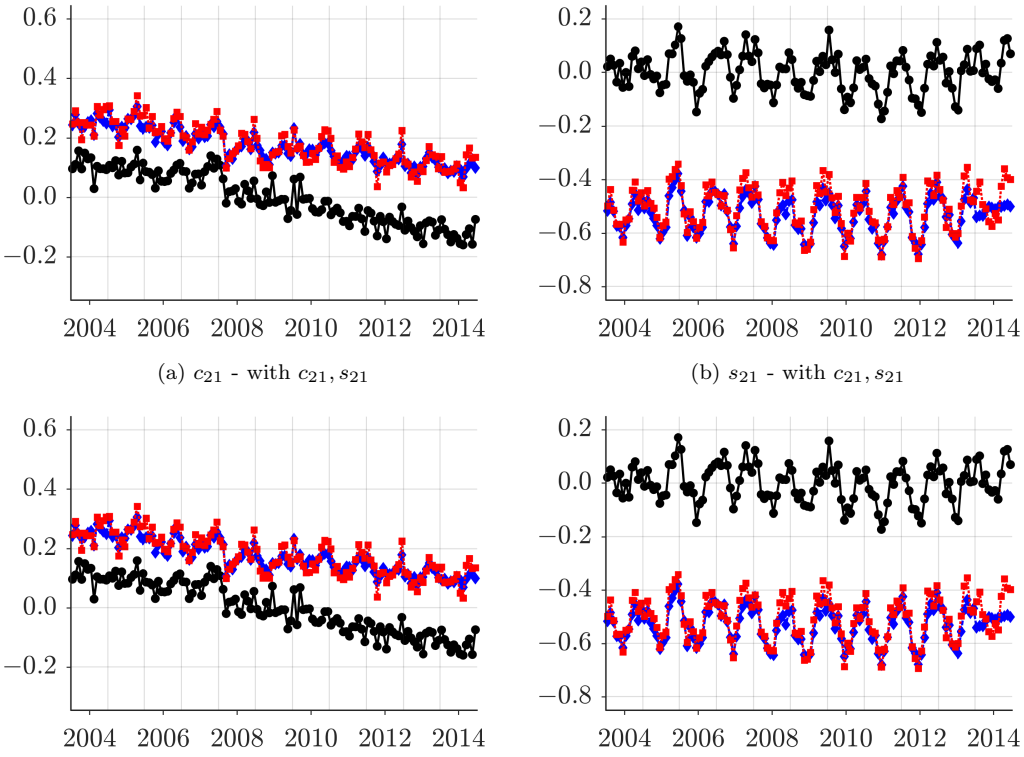

(a) c_{21} - with c_{21}, s_{21}

(b) s_{21} - with c_{21}, s_{21}

(c) c_{21} - with c_{20}, c_{21}, s_{21}

(d) s_{21} - with c_{20}, c_{21}, s_{21}

Figure 5.6: Comparison of the spherical harmonics coefficients $c_{21} \times 10^{+9}$ (left) and $s_{21} \times 10^{+9}$ (right). Reference data of SLR observations (black line). Initial coefficients of Earth's rotation simulation (blue dashed line), see Ch. 3. Calculated coefficients by combining initial coefficients and estimated increments (red dotted line). Data sets were reduced by the mean of the reference series. Determined parameters: (a)/(b) c_{21}, s_{21} and $\boldsymbol{\omega}_0$, (c)/(d) c_{20}, c_{21}, s_{21} and $\boldsymbol{\omega}_0$.

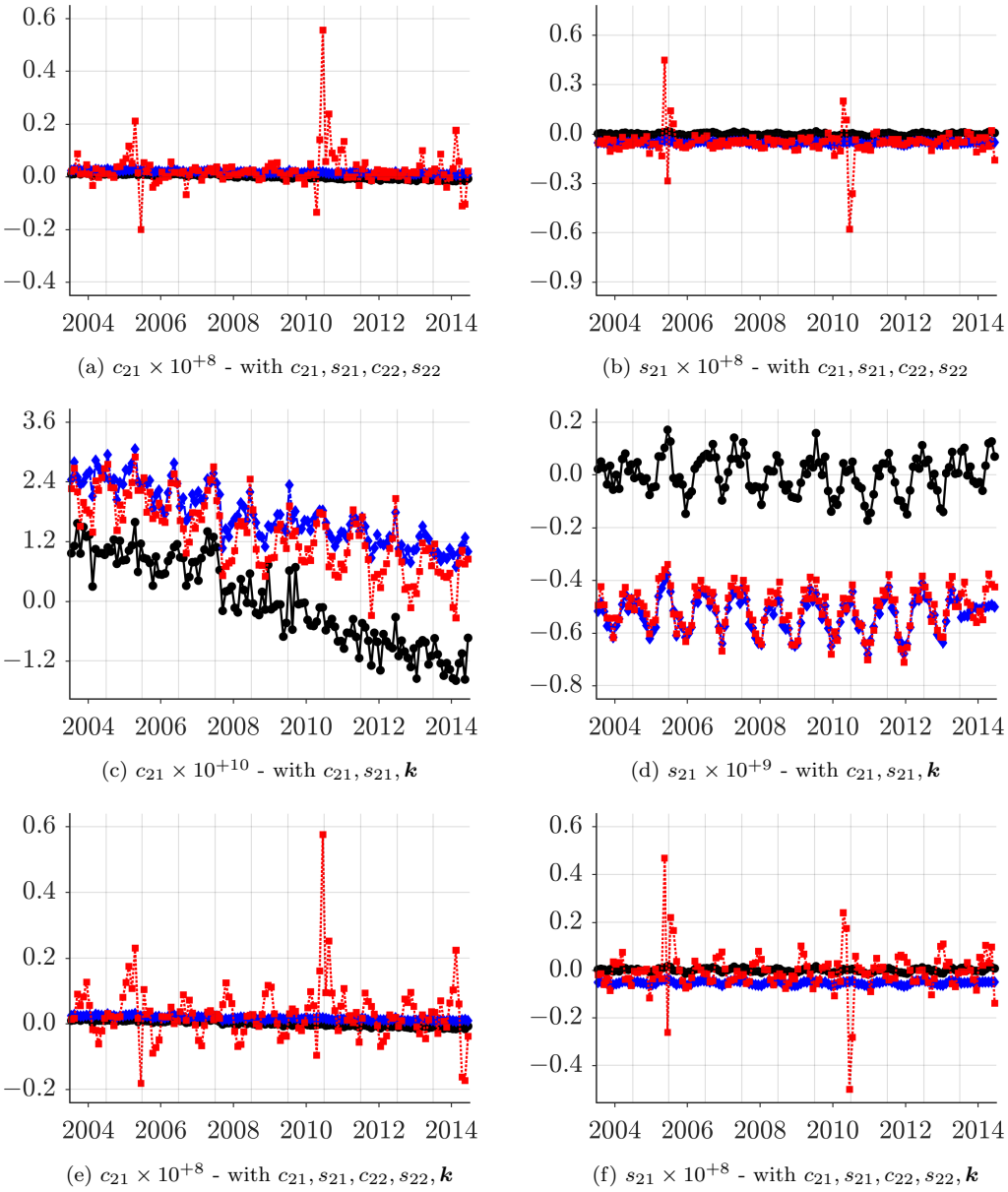

(a) $c_{21} \times 10^{+8}$ - with $c_{21}, s_{21}, c_{22}, s_{22}$

(b) $s_{21} \times 10^{+8}$ - with $c_{21}, s_{21}, c_{22}, s_{22}$

(c) $c_{21} \times 10^{+10}$ - with $c_{21}, s_{21}, \boldsymbol{k}$

(d) $s_{21} \times 10^{+9}$ - with $c_{21}, s_{21}, \boldsymbol{k}$

(e) $c_{21} \times 10^{+8}$ - with $c_{21}, s_{21}, c_{22}, s_{22}, \boldsymbol{k}$

(f) $s_{21} \times 10^{+8}$ - with $c_{21}, s_{21}, c_{22}, s_{22}, \boldsymbol{k}$

Figure 5.7: Comparison of the tesseral spherical harmonics coefficients c_{21} (left) and s_{21} (right). Reference data of SLR observations (black line). Initial coefficients of Earth's rotation simulation (blue dashed line), see Ch. 3. Calculated coefficients by combining initial coefficients and estimated increments (red dotted line). Data sets were reduced by the mean of the reference series. Estimated parameters besides c_{21}, s_{21} and $\boldsymbol{\omega}_0$: (a)/(b) c_{22} and s_{22}, (c)/(d) $\boldsymbol{k}$ and (e)/(f) c_{22}, s_{22} and $\boldsymbol{k}$.

Coefficients c_{22} and s_{22}

The outcome of the sectoral spherical harmonic coefficients c_{22} and s_{22} are listed in Tabs. 5.4 and 5.5. The time series showed an offset by the arithmetic mean values similar to c_{20}. The dimensions of the standard derivations and achieved variances of the estimated increments were larger by factor $\approx 10^5$ than expected. The statistical parameters were consistent throughout various parameter versions, despite the combinations including coefficients c_{21}, s_{21}. Figures 5.8 and 5.9 illustrate the increments in relation to the reference time series of SLR observations and the initial coefficients of the numerical integration. Both existing time series were reduced by the mean of the SLR coefficients and appear as linear lines, due to the size and scaling of the estimated increments. An annual and semi-annual oscillation with strong variations at the beginning of 2007 could be identified for both increments. Combinations with further parameters reduced the occurring bias. However, the obtained results were not meaningful of any adjustment setting, due to the dimension of the variations and variances.

Table 5.4: Statistical parameters of the coefficient increments $\Delta\hat{\boldsymbol{c}}_{22}$ and the obtained certainties $\hat{\sigma}_{c_{22}}$ for implemented parameter combinations.

$\hat{\boldsymbol{x}}\{\boldsymbol{\omega}_0, c_{22}, s_{22}, \dots\}$	$\mu\,(\Delta\hat{\boldsymbol{c}}_{22})$	$s\,(\Delta\hat{\boldsymbol{c}}_{22})$	$\hat{\sigma}_{c_{22}}$
$-$	1.706×10^{-5}	2.4×10^{-5}	$\pm 3.69 \times 10^{-7}$
$\boldsymbol{k}$	2.482×10^{-6}	2.4×10^{-5}	$\pm 1.22 \times 10^{-6}$
c_{20}	1.603×10^{-5}	2.4×10^{-5}	$\pm 4.83 \times 10^{-7}$
c_{21}, s_{21}	-1.047×10^{-6}	4.1×10^{-4}	$\pm 2.27 \times 10^{-5}$
$c_{20}, \boldsymbol{k}$	2.622×10^{-6}	2.4×10^{-5}	$\pm 1.19 \times 10^{-6}$
$c_{20}, c_{21}, s_{21}, \boldsymbol{k}$	-2.109×10^{-5}	4.5×10^{-4}	$\pm 2.49 \times 10^{-5}$
c_{20}, c_{21}, s_{21}	-2.530×10^{-6}	4.1×10^{-4}	$\pm 2.20 \times 10^{-5}$
$c_{21}, s_{21}, \boldsymbol{k}$	-1.842×10^{-5}	4.4×10^{-4}	$\pm 2.57 \times 10^{-5}$

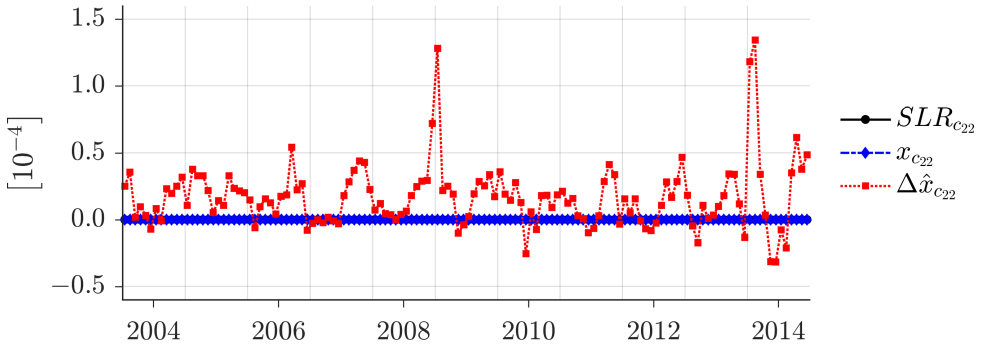

Figure 5.8: Estimated coefficient increments $\Delta\hat{\boldsymbol{c}}_{22}$ (red dotted line) of an adjustment with both second-order parameters and initial starting vector $\boldsymbol{\omega}_0$. Initial coefficients (blue dashed line) for numerical integration of the Earth's rotation vector and published reference data of SLR observations (black line). The initial and reference coefficients were reduced by the arithmetic mean of the SLR series.

The behaviour of both second-order coefficients was similar, especially regarding combinations of first order spherical harmonic coefficients.

Table 5.5: Statistical parameters of the coefficient increments $\Delta\hat{\boldsymbol{s}}_{22}$ and the obtained certainties $\hat{\sigma}_{s_{21}}$ for implemented parameter combinations.

$\hat{\boldsymbol{x}}\{\boldsymbol{\omega}_0, c_{22}, s_{22}, \dots\}$	$\mu\,(\Delta\hat{\boldsymbol{s}}_{22})$	$s\,(\Delta\hat{\boldsymbol{s}}_{22})$	$\hat{\sigma}_{s_{22}}$
–	1.827×10^{-6}	1.6×10^{-5}	3.69×10^{-7}
$\boldsymbol{k}$	1.278×10^{-5}	1.6×10^{-5}	1.22×10^{-6}
c_{20}	1.358×10^{-6}	1.6×10^{-5}	4.40×10^{-7}
c_{21}, s_{21}	4.408×10^{-5}	4.2×10^{-4}	2.27×10^{-5}
$c_{20}, \boldsymbol{k}$	1.269×10^{-5}	1.6×10^{-5}	1.19×10^{-6}
c_{20}, c_{21}, s_{21}	4.747×10^{-5}	4.1×10^{-4}	2.20×10^{-5}
$c_{20}, c_{21}, s_{21}, \boldsymbol{k}$	5.058×10^{-5}	4.6×10^{-4}	2.49×10^{-5}
$c_{21}, s_{21}, \boldsymbol{k}$	4.581×10^{-5}	4.5×10^{-4}	2.57×10^{-5}

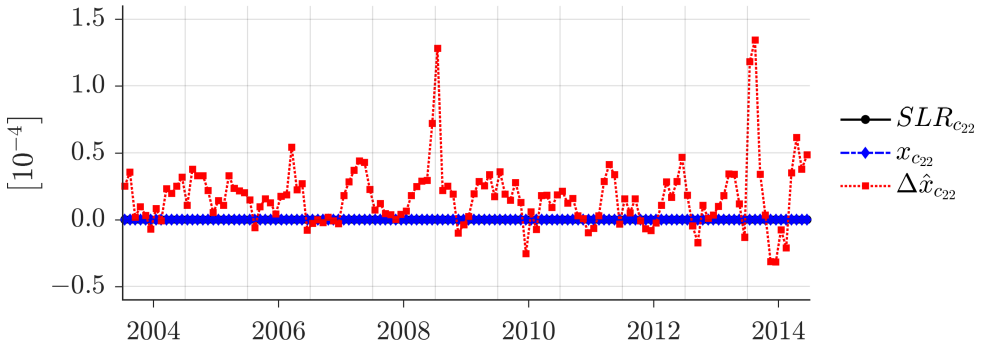

Figure 5.9: Estimated coefficient increments $\Delta\hat{\boldsymbol{s}}_{22}$ (red dotted line) of an adjustment with both second-order parameters and initial starting vector $\boldsymbol{\omega}_0$. Initial coefficients (blue dashed line) for numerical integration of the Earth's rotation vector and published reference data of SLR observations (black line). The initial and reference coefficients were reduced by the arithmetic mean of the SLR series.

5.2 Initial vector elements and Love number

All combinations considered the uncertainties of starting vector of the timer series $\boldsymbol{\omega}_0$, due to the initial value problem at numeric integration of the Earth's rotation vector. Thereby the initial vector consisted of three components:

$$\Delta\hat{\boldsymbol{\omega}}_{\mathbf{0}} = [\Delta\hat{\omega}_0^x \ \Delta\hat{\omega}_0^y \ \Delta\hat{\omega}_0^z]^T \,. \tag{5.1}$$

The increments of the Love number were analogue:

$$\Delta\hat{\boldsymbol{k}} = \left[\Delta\hat{k}^{Re} \ \Delta\hat{k}^{Im}\right]^T \,. \tag{5.2}$$

The spherical harmonic coefficients were cohesively presented monthly to the contrary of the uniquely solved initial vector and Love number increments. The introduction of the initial vector in the algorithm was unavoidable, and the obtained accuracies within the adjustment were sufficient to the defined predefined certainties. Those appear in the weight matrix as reciprocal values and numerical derivations. Table 5.6 lists the results of the estimated initial vector elements. The z-component was overall better determinable concerning

the Earth's rotation vector with smaller variances. Introducing tesseral or sectoral spherical harmonic coefficient as unknown parameters reduced the increment dimensions up to 10^{-2}. The obtained accuracy fluctuated between 10^{-15} rad/s and 10^{-13} rad/s and was below the predefined certainties 10^{-12} rad/s of the algorithm. The zonal spherical harmonic coefficient did have a negative effect on the values of the z-axis.

Table 5.6: Estimated increments of initial vector $\Delta\hat{\boldsymbol{\omega}}_0$ and the posterior accuracies from the covariance matrices in rad/s.

$\hat{\boldsymbol{x}}\{\boldsymbol{\omega}_0, \dots\}$	$\Delta\hat{\omega}_0^x \times 10^{-12}$	$\Delta\hat{\omega}_0^y \times 10^{-12}$	$\Delta\hat{\omega}_0^z \times 10^{-12}$
–	-38.118 ± 0.058	-13.977 ± 0.058	-0.370 ± 0.050
$\boldsymbol{k}$	-13.524 ± 0.040	12.487 ± 0.041	-0.370 ± 0.022
c_{20}	-25.429 ± 0.085	-18.826 ± 0.060	-0.059 ± 0.537
c_{21}, s_{21}	0.515 ± 0.028	-0.407 ± 0.028	-0.370 ± 0.001
c_{22}, s_{22}	0.525 ± 0.027	0.353 ± 0.028	-0.370 ± 0.001
$c_{20}, \boldsymbol{k}$	-12.728 ± 0.040	11.368 ± 0.041	-0.616 ± 0.241
c_{20}, c_{21}, s_{21}	0.515 ± 0.027	0.407 ± 0.027	-0.057 ± 0.015
c_{20}, c_{22}, s_{22}	0.525 ± 0.027	0.358 ± 0.027	-0.056 ± 0.015
$c_{20}, c_{21}, s_{21}, \boldsymbol{k}$	0.562 ± 0.028	0.414 ± 0.028	-0.057 ± 0.015
$c_{20}, c_{22}, s_{22}, \boldsymbol{k}$	0.601 ± 0.027	0.387 ± 0.027	-0.057 ± 0.015
$c_{20}, c_{21}, s_{21}, c_{22}, s_{22}$	0.283 ± 0.039	0.330 ± 0.039	-0.057 ± 0.014
$c_{20}, c_{21}, s_{21}, c_{22}, s_{22}, \boldsymbol{k}$	0.185 ± 0.039	0.310 ± 0.039	-0.057 ± 0.014
$c_{21}, s_{21}, \boldsymbol{k}$	0.563 ± 0.028	0.414 ± 0.028	-0.370 ± 0.001
$c_{21}, s_{21}, c_{22}, s_{22}$	0.283 ± 0.040	0.330 ± 0.040	-0.370 ± 0.001
$c_{21}, s_{21}, c_{22}, s_{22}, \boldsymbol{k}$	0.193 ± 0.040	0.306 ± 0.040	-0.371 ± 0.001
$c_{22}, s_{22}, \boldsymbol{k}$	0.602 ± 0.028	0.387 ± 0.028	-0.370 ± 0.001

Figure 5.10 displays the elements of the covariance matrices of four cases of the initial vector increment. The square root of the principal diagonal are representing the obtained accuracies of the vector elements variances. The similar output proved a stable parameter within the adjustment and observation equation. Maximal and minimal values were varying by $10^{\pm 2}$ rad/s for the x-, y- and by $10^{\pm 1}$ rad/s for the z-components.

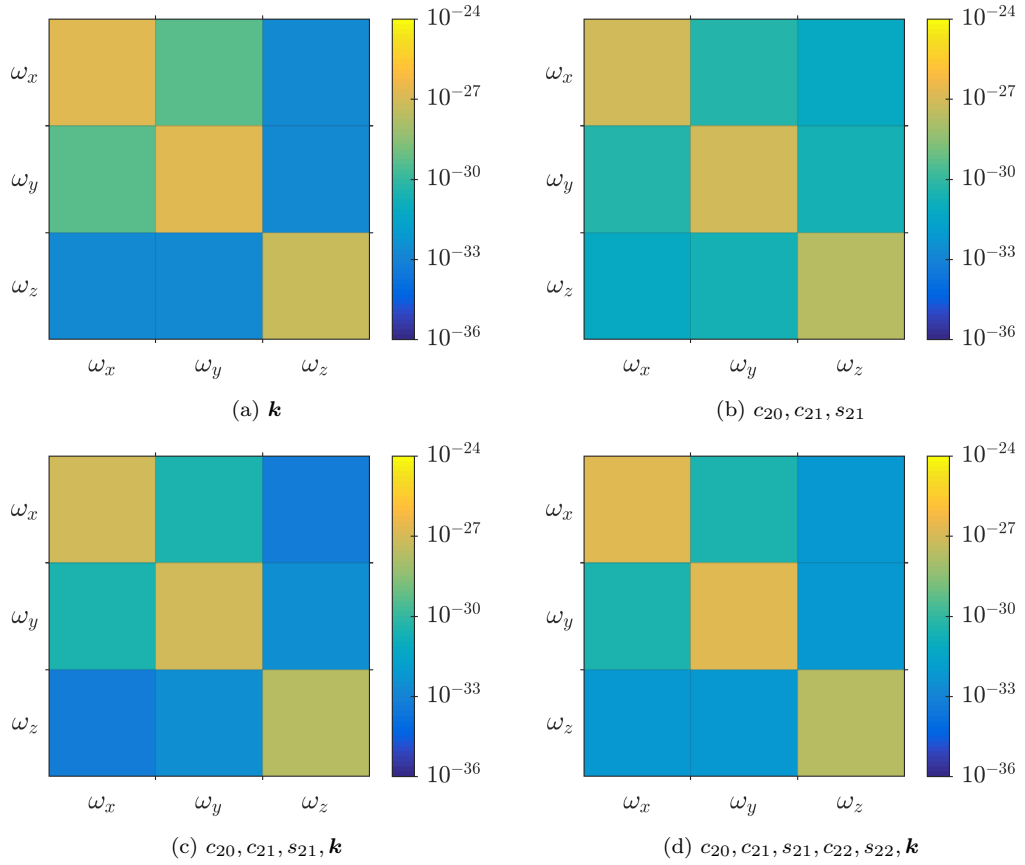

(a) $\boldsymbol{k}$ (b) c_{20}, c_{21}, s_{21}

(c) $c_{20}, c_{21}, s_{21}, \boldsymbol{k}$ (d) $c_{20}, c_{21}, s_{21}, c_{22}, s_{22}, \boldsymbol{k}$

Figure 5.10: Covariance matrices of the initial vector increments $\Delta\hat{\boldsymbol{\omega}}_0$ in $\mathrm{rad}^2/\mathrm{s}^2$ determined with the parameters of: (a) $\boldsymbol{k}$, (b) c_{20}, c_{21} and s_{21}, (c) c_{20}, c_{21}, s_{21} and $\boldsymbol{k}$, (d) $c_{20}, c_{21}, s_{21}, c_{22}, s_{22}$ and $\boldsymbol{k}$ – besides $\boldsymbol{\omega}_0$.

The estimation of Love number parts was introduced to consider variations of the provided values within the adjustment. The increment outcome varied strongly, depending on other unknown parameters as well as the defined numerical derivation interval. The estimated increments are listed in Tab. 5.7. The Love number appeared to be unstable concerning the achieved increments and their corresponding covariance matrix elements. The imaginary part showed smaller variations throughout different versions than the real part, which is affected the most by the introduction of the zonal spherical harmonic coefficient. The covariance matrices with and without spherical harmonic coefficients are

displayed in Fig.. 5.11. The uncertainties increased by adding further parameters. The posterior certainties $\sigma_{\hat{k}} \approx 10^{-2}$ were too inaccurate to make a point about the estimated increments and provided values.

Table 5.7: Estimated Love number increments of $\Delta\hat{k}^{Re}$ and $\Delta\hat{k}^{Im}$ and the posterior accuracies from the covariance matrices.

$\hat{\boldsymbol{x}}\{\boldsymbol{\omega}_0, \boldsymbol{k}, \dots\}$	$\Delta\hat{k}^{Re} \times 10^{-2}$	$\Delta\hat{k}^{Im} \times 10^{-2}$
-	-0.747 ± 0.002	1.850 ± 0.002
c_{20}	86.344 ± 0.682	1.564 ± 0.003
c_{21}, s_{21}	-0.508 ± 0.198	2.962 ± 0.198
c_{22}, s_{22}	1.263 ± 0.129	2.314 ± 0.129
c_{20}, c_{21}, s_{21}	-0.537 ± 0.198	2.903 ± 0.193
c_{20}, c_{22}, s_{22}	1.252 ± 0.134	2.294 ± 0.125
$c_{20}, c_{21}, s_{21}, c_{22}, s_{22}$	-28.751 ± 1.143	-10.991 ± 1.145
$c_{21}, s_{21}, c_{22}, s_{22}$	-27.331 ± 1.170	-8.490 ± 1.182

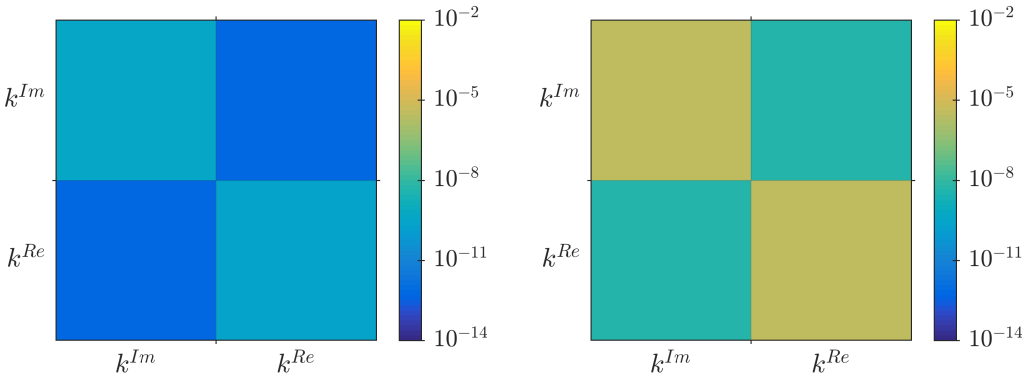

(a) first (b) third

Figure 5.11: Covariance matrices of the Love number's real $\Delta\hat{k}^{Re}$ and imaginary part $\Delta\hat{k}^{Im}$ determined using the parameters of: (a) $\boldsymbol{\omega}_0$ and $\boldsymbol{k}$, and (b) $\boldsymbol{\omega}_0, \boldsymbol{k}, c_{20}, c_{21}$ and s_{21} – besides the Love number $\boldsymbol{k}$.

5.3 Coherent consideration

Four specific cases are defined in Tab. 5.8 for reasons of legibility.

Table 5.8: Final cases of estimated parameter combinations.

	$\boldsymbol{\omega}_0$	c_{20}	c_{21}	s_{21}	c_{22}	s_{22}	$\boldsymbol{k}$
1st case	✗						✗
2nd case	✗	✗	✗	✗			
3rd case	✗	✗	✗	✗			✗
4th case	✗	✗	✗	✗	✗	✗	✗

The coefficients of c_{20}, c_{22} and s_{22} were not suitably determined relating to the Earth's rotation vector with the use of its simulation. The zonal spherical harmonic coefficient c_{20} was consistently fraught by an offset. Even though the mean free temporal variation's dimensions were in good agreement to the reference solution, the determined certainties appeared larger than their increments. Introducing additional spherical harmonic coefficients had a stabling effect on the zeroth order estimations without significant enhancement of their biases.
The contrary applied to the appropriate values of coefficient c_{21} and s_{21}. The achieved results got more inaccurate by adding further parameters, especially in combinations with the sectoral spherical harmonic coefficients. The most reasonable product was obtained by adding the Love number. Whereby the alterations mainly occurred at the cosine coefficient, while the sine coefficient remained unchanged. The variances were in good agreement with their comparable SLR accuracies.
Estimations of second-degree and -order coefficients were not viable throughout all parameter combinations. The determined certainties as well as increments were by an average factor 10^5 larger than required.
The estimation of the initial vector was necessary, due to the initial value problem at the numeric integration. The achieved variances were adequate and improved by introducing further parameters unlike the Love number, which was only rational in combination with coefficient c_{21} and s_{21}. Both uniquely determined parameters had no additional benefit in the default algorithm of this application.

Therefore the estimation of the third case parameters was recommended regarding a determination of spherical harmonic coefficients concerning the Earth's rotation. The best correlation was proven by the tesseral coefficients. Although the estimation of coefficient c_{20} increased the computation time, it should be studied for the gain of further information regarding its offsets. Figure 5.12 illustrates the covariance matrices of four cases. Adding coefficient c_{20} had no negative consequences for other parameters and was considered as stabilisation, despite the mentioned scientific purpose.

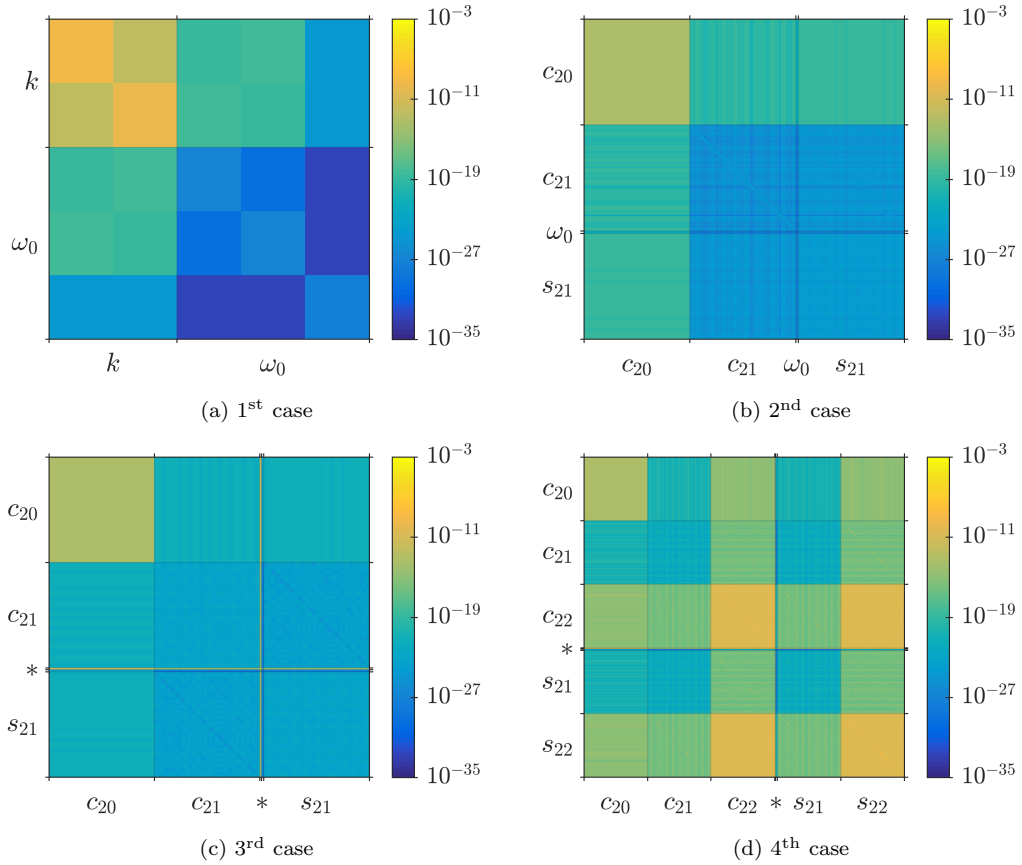

(a) 1st case (b) 2nd case

(c) 3rd case (d) 4th case

Figure 5.12: Covariance matrices of least square adjustments for the four final cases in Tab. 5.8. Asterisk (*) stands for the Love number parts k^{Im}, k^{Re} and initial vector $\omega_0^x, \omega_0^y, \omega_0^z$ at (c) and (d). Variances presented in $\mathrm{rad}^2/\mathrm{s}^2$ for the rotation vector and unit less for the love number and harmonic coefficients.

5.4 Further considerations

Additional investigations were realised by drawing on the results of the adjustment verification in Sec. 4.5. A connection was recognised between the estimated values and derivation elements. Therefore, the interval sizes of the parameters were modified in this manner. The numerical derivation differences are listed in Tab. 5.9 for each parameter. The adjusted step size is stated as $\Delta\tilde{p}$ according to the obtained variances of the first determination using Δp. Thereby the more inaccurate parameters were affected and further diminished their increments as displayed in Fig. 5.13 for the covariance matrices.

Table 5.9: Interval increments of the numeric derivation.

parameter	Δp	$\Delta\tilde{p}$
$\omega_x, \omega_y, \omega_z$	10^{-12}	10^{-14}
c_{20}	10^{-11}	10^{-8}
c_{21}, s_{21}	10^{-11}	10^{-12}
c_{22}, s_{22}	10^{-11}	10^{-6}
k^{Re}, k^{Im}	10^{-4}	10^{-3}

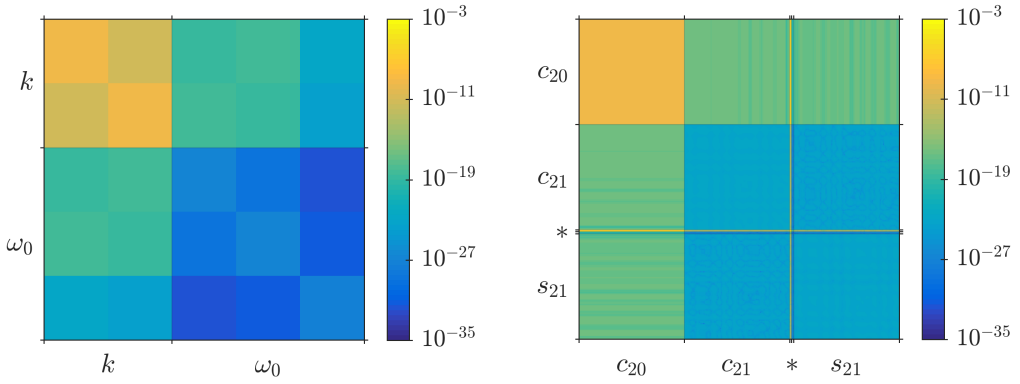

(a) 1^{st} case (b) 2^{nd} case

Figure 5.13: Covariance matrices of adjustment with adjusted numerical derivation interval $\Delta\tilde{p}$. Estimated parameters of: (a) the 1^{st} case and (b) the 3^{rd} case – asterisk (*) stands for the Love number parts k^{Im}, k^{Re} and initial vector $\omega_0^x, \omega_0^y, \omega_0^z$. Variances presented in rad^2/s^2 for the rotation vector and unit less for the love number and harmonic coefficients.

Additionally, the numeric derivation interval was set as small as possible without numerical warnings or errors by the software. Even though the calculation was theoretically possible, the determined increments were too small to detect any alterations to the approximated coefficients, similar to the standalone versions of the tesseral spherical harmonic coefficients.

The method of iteration was further considered, assuming that the increments would approach zero. Therefore the standalone versions of each coefficient degree were estimated in combination with the initial value. Absolute increments of this approach are characterized in Fig. 5.14.

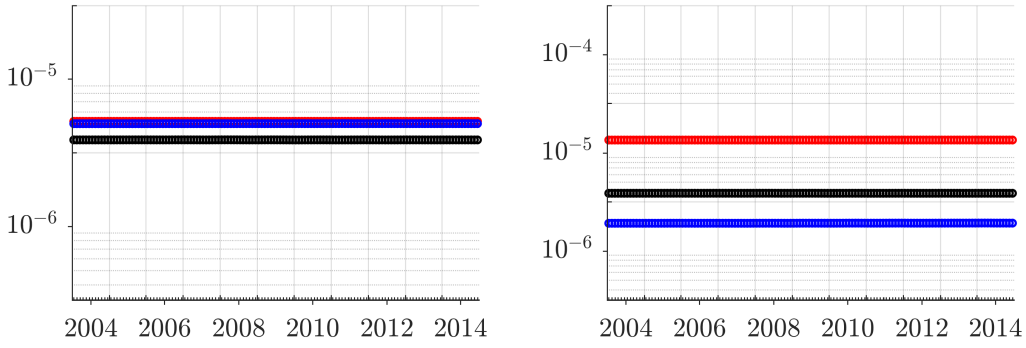

(a) c_{20} - with constant initial value

(b) c_{20} - with iterating initial value

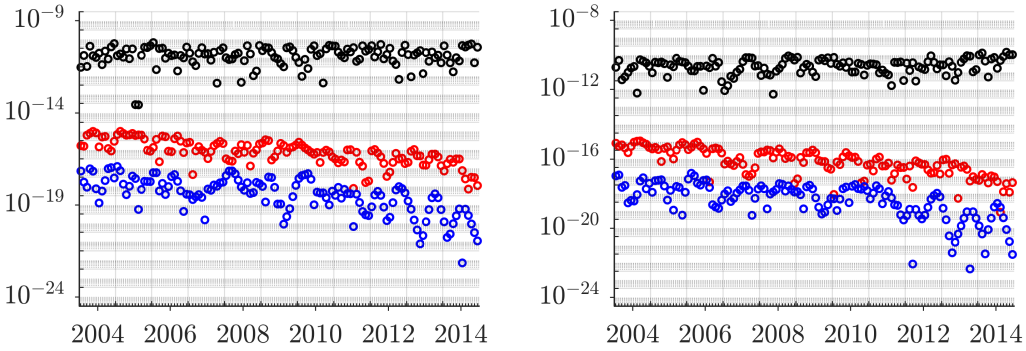

(c) c_{21} - with constant initial value

(d) s_{21} - with constant initial value

Figure 5.14: Absolute values of estimated spherical harmonic coefficient increments of first (black circles), second (red circles) and third (blue circles) iteration. Increments of: (a) c_{20} - estimation with constant initial value, (b) c_{20} - estimation with iterating initial value, (c) c_{21} - estimation with s_{21} and constant initial value, (d) s_{21} - estimation with c_{21} and constant initial value.

The occurring offsets of the coefficients remained in similar dimensions. The assumption that signs were switching for each iteration was not confirmed, as Tab. 5.10 proves. The increments of coefficient c_{21} and s_{21} decreased as expected. Second-order parameter of c_{22} as well as of s_{22} did not improve either to fit the expected dimensions. Iterated parts of the Love number fluctuated by the same dimensions. In contrast to the iteration results of initial elements which decreased rapidly. The topic of iteration was not investigated in detail. The collected information retained unchanged for the estimating coefficient and determinability.

Table 5.10: Iteration results of spherical harmonic coefficients of each parameter in combination with constant $\boldsymbol{\omega}_0$.

x	$\mu(\Delta\hat{\boldsymbol{x}})\vert_1$	$\mu(\Delta\hat{\boldsymbol{x}})\vert_2$	$\mu(\Delta\hat{\boldsymbol{x}})\vert_3$
$c_{20}\{\boldsymbol{\omega}_0, c_{20}\}$	-3.877×10^{-6}	-5.182×10^{-6}	-4.999×10^{-6}
$c_{21}\{\boldsymbol{\omega}_0, c_{21}, s_{21}\}$	6.662×10^{-12}	-3.557×10^{-18}	-7.887×10^{-20}
$s_{21}\{\boldsymbol{\omega}_0, c_{21}, s_{21}\}$	2.485×10^{-11}	-7.863×10^{-18}	-3.989×10^{-20}
$c_{22}\{\boldsymbol{\omega}_0, c_{22}, s_{22}\}$	1.706×10^{-5}	9.988×10^{-7}	-1.384×10^{-7}
$s_{22}\{\boldsymbol{\omega}_0, c_{22}, s_{22}\}$	1.827×10^{-6}	-1.204×10^{-6}	-1.909×10^{-7}

6 Conclusion

The approach to determine second-degree spherical harmonic coefficients in relation to the Earth's rotation vector was researched using the differential Euler-Liouville equation. Therefore the formula was adapted to simulate an Earth's rotation vector and further estimate the gravity field parameters per month of the inertia tensor – second-degree spherical harmonic coefficients.
The presented parameter configurations in this thesis were validated by SLR observations and showed that the tesseral second-degree coefficients c_{21} and s_{21} were the most sufficient in terms of temporal variations as well as computed variances. The pole-flattening coefficient c_{20} did not reach the required accuracies and contained a yet unexplained offset. Establishing the bias's origin could improve the determined results since the temporal variations of the constant trend reduced increments indicated adequate differences. Contrary to the second-order coefficients c_{22} and s_{22}, which are fraught by consistent offsets at every combination and uncertainties twice as large as their reference solutions.
The obtained dimensions of the zeroth- and first-order coefficient depended strongly on the added parameters, whereby the uncertainties of the first one decreased, whereas those of the second ones increased. The best coherence to the rotation vector was presented by the coefficients c_{21} and s_{21} due to their consistency and precise results, except for combinations including sectoral harmonic coefficients.

Although the achieved increments did not lead to a significant improvement of the approximated coefficients since they were too small in relation to the differences between the initial and reference harmonic coefficients. Further, it was assumed that the approximated coefficients caused the occurring bias at coefficients c_{20}, which remains to be investigated. Therefore additional considerations of the used initial gravity field models may be required.
Furthermore, correcting the modelled rotation vector during its integration would reduce differences to the observations with the use of a filter algorithm.

6 Conclusion

One of the acknowledged error sources was the simulation of the rotation vector. Correcting the simulated rotation vector during its integration could reduce differences between the observation and simulation by using a filter algorithm. Whereby the accuracies and temporal behaviour of the measurements are considered for each period.

Bibliography

Bizouard, C. and D. Gambis (2019). *The combined solution C04 for Earth Orientation Parameters consistent with International Terrestrial Reference Frame 2008*. GFZ Data Services. URL: file:///D:/Downloads/C04.guide.pdf (visited on 03/15/2019) (cit. on p. 13).

Cheng, M., J. C. Ries, and B. D. Tapley (2011). "Variations of the Earth's figure axis from satellite laser ranging and GRACE." In: *JGR: Solid Earth* 116. DOI: 10.1029/2010JB000850 (cit. on pp. 33, 34).

Dehant, V., P. Defraigne, and J. M. Wahr (1999). "Tides for a convective Earth." In: *JGR: Solid Earth* 104. DOI: 10.1029/1998JB900051 (cit. on p. 12).

Dehant, V. and P. M. Mathews (2015). *Precession, nutation and wobble of the Earth*. First. Cambridge University Press. ISBN: 9781107092549 (cit. on pp. 2, 3, 9).

Dobslaw, H. and R. Dill (2018). "Predicting Earth Orientation Changes from Global Forecasts of Atmosphere-Hydrosphere Dynamics." In: *Advances in Space Research* 61 (4). DOI: 10.1016/j.asr.2017.11.044 (cit. on p. 15).

Flechtner, F., H. Dobslaw, and E. Fagiolini (2014). *AOD1B Product Description Document for Product Release 05*. Rev. 4.2 (cit. on p. 13).

GGOS (2016). *Global Geodetic Observing System*. Services. URL: http://wwww.ggos.org/ (cit. on p. 1).

GOCO (2019). *Gravity Observation Combination*. URL: http://wwww.goco.eu (cit. on p. 33).

Griffiths, D. F. and D. J. Higham (2010). *Numerical methods for ordinary differential equations*. Springer. ISBN: 9780857291486 (cit. on p. 16).

IERS (2013). *International Earth Rotation and Reference Systems Service*. URL: http://wwww.iers.org (cit. on pp. 3, 6, 27, 32).

JPL (2014a). *Jet Propulsion Laboratory*. Ephemerides. California Institute of Technology. URL: https://ssd.jpl.nasa.gov/?ephemerides (visited on 01/16/2019) (cit. on pp. 3, 13).

JPL (2014b). *Jet Propulsion Laboratory*. Gravity Recovery And Climate Experiment - Oblateness. California Institute of Technology. URL: http://grace.jpl.nasa.gov (visited on 01/22/2019) (cit. on pp. 33, 34).

Koch, K.-R. (1999). *Parameter estimation and hypothesis testing in linear models*. Second. Springer. ISBN: 9783540652571 (cit. on p. 18).

Lieske, J.H. et al. (1977). *Expressions of the Precession Quantities Based upon the IAU (1976) System of Astronomical Constants* (cit. on p. 3).

Mayer-Gürr, T. et al. (2016). *ITSG-Grace2016 - Monthly and Daily Gravity Field Solutions from GRACE*. GFZ Data Services. DOI: 10.5880/icgem.2016.007 (cit. on p. 13).

Moritz, H. and I. I. Mueller (1987). *Earth Rotation: Theory and Observation*. Ungar. ISBN: 9780804446716 (cit. on pp. 1, 4, 9, 10).

Petit, G. and B. Luzum (eds.) (2010). *IERS Conventions (2010)*. Frankfurt am Main: Verlag des Bundesamts für Kartographie und Geodäsie. 179 pp. ISBN: 3-89888-989-6. URL: http://www.iers.org/TN36 (visited on 03/15/2019) (cit. on p. 13).

Savcenko, R. and W. Bosch (2012). *EOT11a - Global Empirical Ocean Tide model from multi-mission satellite altimetry*. DGFI Report No.89. Deutsches Geodätisches Forschungsinstitut (DGFI). DOI: 10.1594/PANGAEA.834232 (cit. on p. 13).

Seitz, F. (2004). "Atmosphärische und ozeanische Einflüsse auf die Rotation der Erde." PhD thesis (cit. on pp. 6, 11).

Seitz, F. and H. Schuh (2010). "Earth Rotation." In: *Sciences of geodesy - I: Advances and future directions*. Ed. by Guochang Xu. Springer, pp. 185–227. ISBN: 978-3-642-11741-1 (cit. on p. 8).

The MathWorks, Inc (2019). *MATLAB documentation*. URL: https://de.mathworks.com/help/matlab/index.html (cit. on p. 24).